meteorology

MDPI

Article

Variability of the Diurnal Cycle of Precipitation in South America

Ronald G. Ramírez-Nina *,†, Maria Assunção Faus da Silva Dias and Pedro Leite da Silva Dias

Departamento de Ciências Atmosféricas, Instituto de Astronomia, Geofísica e Ciências Atmosféricas, Universidade de São Paulo, São Paulo 05508-090, Brazil; maria.silvadias@iag.usp.br (M.A.F.d.S.D.); pedro.dias@iag.usp.br (P.L.d.S.D.)

* Correspondence: ronald.ramirez.nina@usp.br; Tel.: +55-1197822-2448

† Current address: Rua do Matão, 1226-Butantã, São Paulo 05508-090, Brazil.

Abstract: A seasonal climatology of the diurnal cycle of precipitation (DCP) and the assessment of its observed trend since the beginning of the 21st century using the IMERG product are performed for South America (SA). Its high spatial–temporal resolution ($\Delta x = 0.1°$, $\Delta t = 0.5$ h) enables the examination of the fine-scale features of the DCP associated with the complex physical characteristics of SA. Using 20 years of precipitation rate data, diurnal and semi-diurnal scale processes are analyzed through harmonic analysis. Diurnal metrics—including the hourly mean precipitation rate, normalized amplitude, and phase—are employed to quantify the DCP. The results indicate that large-scale mechanisms, such as the South American Monsoon System (SAMS), seasonally modulate the DCP. These mechanisms in combination with local factors (e.g., land use, topography, and water bodies) influence the timing of peak and intensity of precipitation rates. Cluster analysis identifies regions with homogeneous DCP; however, some distant regions are classified as homogeneous, suggesting that local-scale physical processes triggering precipitation onset operate similarly across these regions (e.g., thermally induced local circulations). The trend analysis of the DCP reveals that, over the past 20 years, the tropical region of SA has undergone changes in the intensity and hourly distribution of this fine-scale climate variability mode. This trend is heterogeneous in space and time and is possibly associated with land-use changes.

Keywords: diurnal cycle of precipitation; South America; IMERG; heterogeneity; trend

check for updates

Academic Editors: Paul D. Williams and Edoardo Bucchignani

Received: 11 March 2025
Revised: 30 April 2025
Accepted: 15 May 2025
Published: 21 May 2025

Citation: Ramírez-Nina, R.G.; da Silva Dias, M.A.F.; da Silva Dias, P.L. Variability of the Diurnal Cycle of Precipitation in South America. *Meteorology* **2025**, *4*, 13. https://doi.org/10.3390/meteorology4020013

Copyright: © 2025 by the authors. Licensee MDPI, Basel, Switzerland. This article is an open access article distributed under the terms and conditions of the Creative Commons Attribution (CC BY) license (https://creativecommons.org/licenses/by/4.0/).

1. Introduction

Characterizing the diurnal cycle of precipitation (DCP) over South America (SA) is a major challenge, as it results from the complex interaction of multiple multiscale physical processes. The presence of a rugged topography due to the Andes mountain range, along with a heterogeneous surface composed of water bodies, forests, savanna-like areas, urban centers, and agricultural lands, generates thermally induced local circulations [1–8], which in turn modify the DCP.

From the perspective of numerical weather and climate modeling, the DCP has long been a subject of interest in evaluations of its behavior across the entire SA for several decades for both General Circulation Models (GCMs; [9–13]) and regional models ([5,14,15], end references therein). The literature has focused on the evaluation of physical parameterization schemes for convection, comparisons between them and between models that explicitly resolve convection, the refinement of spatial (Δx) and temporal (Δt) resolution, and assessing super-parameterizations embedded within GCMs. Early in this

century, ref. [9] evaluated the performance of short- and long-term runs of the European Centre for Medium-Range Weather Forecasts (ECMWF) forecast model in the Rondônia region, Northern Brazil. The authors observed that the model reproduced precipitation a few hours after sunrise, underestimated hourly precipitation, and failed to reproduce nighttime and early morning rainfall. They attributed the errors in the timing and onset of precipitation to the ECMWF convection scheme and noted that the model failed to simulate mesoscale convective systems (MCSs). Ref. [10] analyzed the performance of DCP simulations in global climate models (both hydrostatic and non-hydrostatic) by comparing different spatial resolutions and convective parameterizations. They emphasized that when convection remains parameterized, few significant improvements are observed with increasing spatial resolution (Δx). In addition, they found that models that solve for convection explicitly better simulate the phase of the DCP and the precipitation induced by local circulations, such as sea breeze and valley–mountain flows, compared to models with parameterized convection. These results are in agreement with the findings of [11,12], who evaluated the global-scale DCP using data from the Coupled Model Intercomparison Project Phase 5 (CMIP5) and 6 (CMIP6), as well as the ECMWF Reanalysis V5 (ERA5, [16]), against satellite-derived hourly precipitation products. In a more recent study, ref. [13] evaluated the performance of the DCP over the Amazon Basin (AB) using both a CMIP6 ensemble and a non-hydrostatic model with explicit convection, reporting results consistent with previous studies. However, the authors highlighted that certain processes are still not adequately represented by the model with explicit convection, even when the spatial resolution is refined, indicating that increasing resolution (i.e., reducing grid spacing Δx) does not necessarily lead to significant improvements. Regarding regional models, studies such as [5] highlighted the role of thermally induced mesoscale circulations in modulating the DCP over the Central Andes of Peru. Ref. [14] evaluated the performance of two regional climate models over SA, identifying five regions with predominant DCP characteristics: the Amazon, the Brazilian Highlands, the northeastern coast of South America, the Andes, and the western coast of Colombia. The study also noted that nocturnal precipitation, primarily generated by MCSs, is not adequately represented over the Amazon and La Plata Basin. More recently, ref. [15] used simulations from two regional models to compare runs with explicit convection and convective parameterization schemes over southeastern SA. The authors found that convection-permitting models are better able to reproduce the observed diversity of DCP patterns captured by meteorological stations.

Observational studies of the DCP using in situ weather stations [2–4,7,15] and ground-based meteorological radars [17,18] have been conducted in different regions of SA. In southeastern SA, using observations of accumulated precipitation at 3-h intervals from 54 meteorological stations, ref. [15] found that DCPs are highly diverse. These DCPs exhibit variations in the timing of peak precipitation and frequently display a double peak. The study highlighted that the most intense precipitation accumulations are associated with nocturnal rainfall, with peaks usually observed at 9:00 local time. Several works have been carried out in the tropical region of SA, especially in the AB [2,4,7,17,18]. Ref. [2], through a network of 24 meteorological stations distributed across the Brazilian Amazon, demonstrated that there is a high spatial and temporal variability of the DCPs. The study emphasizes the seasonality of the DCP in the Brazilian Amazon and suggests that systems forming along the Atlantic coast are only able to propagate as far as central Amazonia. Additionally, the authors mention the possible displacement of systems from the Andes toward central Amazonia, likely associated with thermally induced local circulations. Ref. [4] observed the influence of large Amazonian rivers, rainforest cover, and the urban area of Manaus (Amazonas State, Brazil) on the modulation of the frequency, intensity, and timing of the DCP peak. Their study shows that the highest precipitation accumulations

are observed at stations located within the rainforest, compared to those in the city of Manaus. The authors mentioned that the frequency of rainfall events is greater during the rainy season than in the dry season, highlighting that the higher accumulations during the rainy season result primarily from the increased frequency of rainfall events rather than from greater intensities. Furthermore, the study highlighted the role of thermally induced local circulations (e.g., river breezes) as important triggers for the development of rainfall-producing systems. In Colombia, in the tropical Andes, using hourly precipitation records from 51 meteorological stations, ref. [3] showed that the DCP exhibits heterogeneous characteristics—such as intensity, frequency, and timing of the maximum—even among nearby stations. The authors attributed this heterogeneity to the interaction of local factors (e.g., topography) with both synoptic-scale and local-scale dynamics. In addition to the pronounced seasonality of the diurnal cycle of precipitation (DCP), they found that low-frequency oscillations, such as the Madden–Julian Oscillation (MJO) and the phases of the El Niño–Southern Oscillation (ENSO), can modulate the DCP in the tropical Andes of Colombia. In the Medellín Valley (Colombia), ref. [19] identified a seasonal phase shift in the DCP, resulting in a bimodal behavior caused by the superposition of two unimodal DCPs throughout the year: one occurring in the afternoon (October–April) and the other at night (May–September). The authors also highlighted the influence of low-level jets (LLJs) and afternoon evaporation processes on the formation of mesoscale convective systems (MCSs), thereby contributing to the heterogeneous behavior of the DCP. In Ecuador, between the Amazon lowlands and southern region of the country, ref. [20] analyzed the diurnal cycle of precipitation (DCP) using a K-band rainfall radar profiler, identifying two distinct peaks: a more intense one near dawn and a secondary one during the afternoon hours. This study attributed the near-dawn peak to MCSs formed overnight in the Amazon and subsequently transported toward the Ecuador by prevailing easterly winds in the middle troposphere. The secondary afternoon peak is associated with convection induced by solar heating, which produces differential heating between the valleys and the slopes of the Andes, favoring the formation of MCSs. Also in Ecuador, in the upper equatorial Andes, using data from 80 meteorological stations, ref. [7] investigated the diurnal and seasonal cycles of precipitation by applying clustering techniques to group similar precipitation patterns. Their findings reveal that the DCP and seasonal cycle are highly heterogeneous and strongly dependent on the altitude of the region studied. They identified unimodal and bimodal precipitation cycles, as well as groups with no clearly defined DCP regime, along with notable variations in intensity, frequency, and timing of peak occurrence. In the Central Andes region of Peru, ref. [18] found that convective activity is dominant during the afternoon and early evening, characterized by more intense precipitation and larger raindrops. Furthermore, they observed that stratiform rainfall occurs mainly between nighttime and early morning hours. The aforementioned studies provide important insights of the DCP, including aspects such as frequency of occurrence, intensity, timing of peaks, distribution type (e.g., unimodal or bimodal), seasonality, and the influence of low-frequency oscillations (e.g., MJO and ENSO), among others. However, these studies are limited by factors such as sparse spatial coverage, short or discontinuous observation periods, and a focus on specific localized areas.

Studies of the DCP using satellite precipitation products ([11,12,14,21], and references therein) help overcome gaps in the spatial coverage and limitations associated with the discontinuous sampling of in situ weather station networks and ground-based meteorological radars. However, satellite precipitation products are subject to sampling uncertainties associated with their sensors, which indirectly estimate precipitation (e.g., see [22–25], regarding the IMERG satellite precipitation product). Despite their limitations, key features of the DCP have been identified across different regions of SA and the adjacent Atlantic

and Pacific Oceans. Over SA, the DCP is more pronounced than over the Atlantic and Pacific Oceans ([11,12,14,21], and references therein). The timing of precipitation peaks over SA ranges from the afternoon (e.g., in coastal regions) to the evening (e.g., in the central region of SA), whereas over the Atlantic and Pacific Oceans, peaks occur between dawn and morning ([11,12,14,21], and references therein). It has been observed that the diurnal amplitude over SA is stronger in summer than in winter ([14,21,26], and references therein), with the frequency of rainfall events playing a more significant role than intensity in determining hourly accumulations [21,26]. In a more recent study, [8] found that the DCP in the Amazon Basin (AB) is heterogeneous both spatially and temporally. The authors highlight that large-scale physical mechanisms, such as the South American Monsoon System (SAMS; [27–31]), modulate the temporal and spatial variability, while local factors influence the intensity, diurnal distribution, and timing of peak precipitation rates.

As demonstrated in previous studies, satellite-based precipitation products offer valuable insights due to their continuous spatial and temporal coverage, enabling the identification of key features of the DCP. While ground-based networks of weather stations and radars—often located in or near urban centers—capture local influences on precipitation, satellite products make it possible to investigate remote regions (e.g., mountainous areas, forests, and oceans), capturing both local influences and their interactions with regional- and global-scale processes. Studying the DCP from a continental perspective enhances our ability to visualize and understand the complex interactions that occur throughout the day, the life cycles of the principal systems acting in SA, and to identify the typical physical mechanisms and processes operating in different regions of the continent. Recognizing these mechanisms and the physical processes that trigger the formation of specific rain-producing systems will enable the regionalization of the variability of the DCP into homogeneous groups, based on characteristics such as intensity, diurnal distribution, and timing of precipitation rate peaks.

The objective of this study is to quantify the DCP seasonally through diurnal metrics such as hourly mean precipitation rate, diurnal distribution of precipitation rate, and the timing of peak occurrence for SA during the period 2001–2020. Homogeneous areas of the DCP are identified based on the diurnal metrics to establish common physical mechanisms and processes affecting these areas. The trend of the DCP in SA since the beginning of the current century is examined through diurnal metrics. For this purpose, the IMERG research product is used, which provides continuous temporal and spatial coverage over all of SA, overcoming the limitations of the sparse weather station network in the region.

2. Materials and Methods

2.1. Study Area

The study area of this work is the South American (SA, 57° S–13° N/83° W–33° W) continent, consisting of 13 countries: Argentina, Bolivia, Brazil, Chile, Colombia, Ecuador, French Guiana, Guiana, Paraguay, Peru, Suriname, Uruguay, and Venezuela. SA is bordered to the north by the Caribbean Sea, in the west and south by the Pacific Ocean, and to the east by the Atlantic Ocean. On its western side, SA has a mountain range known as the Andes, which is the longest continental mountain range in the world and exhibits strong topographic gradients (Figure 1A). In addition to the Andes Mountains, SA has large urban centers, forest areas, grasslands, river systems giving rise to watersheds, farmlands, and arid areas. The complex multiscale interactions of different atmospheric phenomena in combination with climatic factors give rise to a non-homogeneous behavior of the diurnal cycle of precipitation throughout SA (Figure 1C–J).

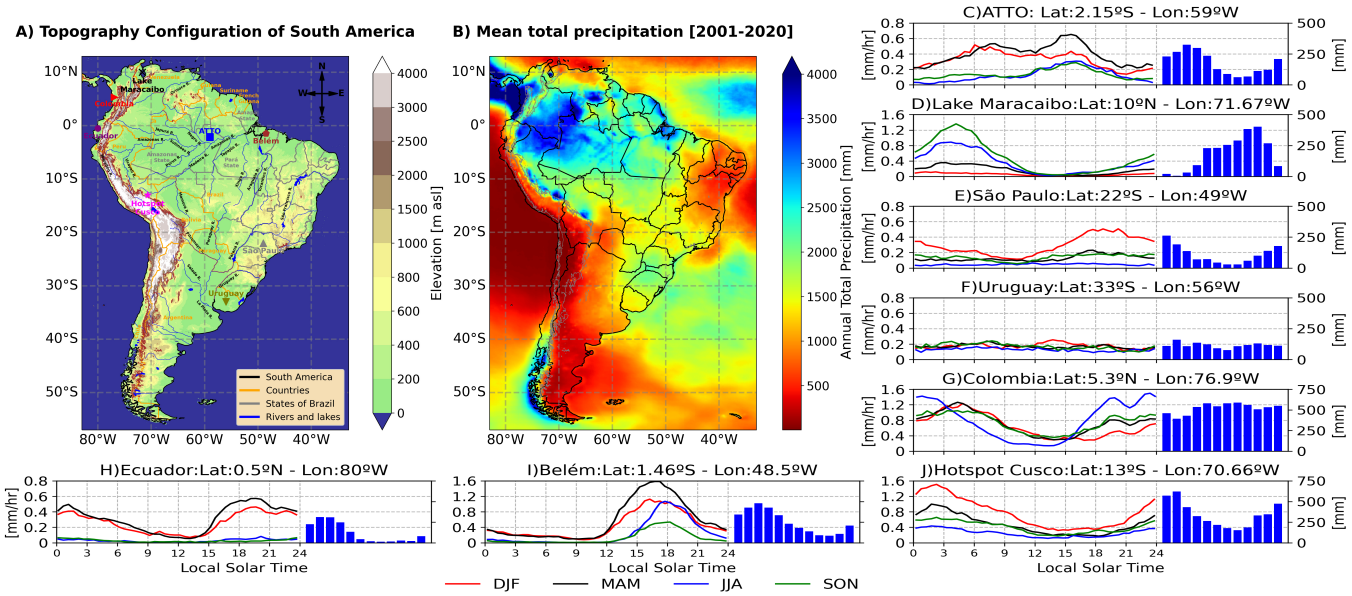


Figure 1. (**A**) South America (SA) topography (depicted in shades) with main rivers (blue lines), where the gray line delimits the states of Brazil and countries, the black line is the outline of South America and the symbols within SA represent the locations from which the IMERG product precipitation rate time series shown in the panels were extracted. (**B**) Spatial distribution of the mean annual total precipitation (mm). The gray line extending from the extreme south to the extreme north of SA marks the 1500 m a.s.l. elevation of the Andes and other highlands regions. Panels (**C**–**J**) display the mean diurnal cycle of precipitation on the left side (colored lines) and the mean annual cycle on the right side (bars), with months from January to December ordered left to right. (**C**) ATTO (Amazon Tall Tower Observatory, Brazil), (**D**) Lake Maracaibo (Venezuela), (**E**) São Paulo (Brazil), (**F**) Uruguay, (**G**) Colombia, (**H**) Ecuador, (**I**) Belém (Brazil), and (**J**) Hotspot Cusco (Peru). Curves represent the average diurnal cycle of precipitation for periods December to February—DJF (red), March to May—MAM (black), June to August—JJA (blue) and September to November—SON (green). The data are derived from IMERG products, using a 30 min temporal resolution for the diurnal cycle and daily resolution for computing both the mean annual cycle and the total annual precipitation over the period 2001–2020.

Precipitation in SA varies strongly in both space and time as a result of multiple multiscale physical processes that interact with each other and with the surrounding environment. In terms of mean annual total precipitation (Figure 1B), the lowest accumulations (values below 500 mm/year) are observed in Southern Argentina, Central and Northern Chile, along the coastal region of Peru, and in Northeastern Brazil. On the other hand, the highest annual totals (values above 2500 mm/year) are found in the tropical region of SA, especially in the Amazon Basin (AB). In the northwestern region of the AB, and along the eastern slopes of the Central Andes in Peru and Bolivia—a region that hosts precipitation hotspots [5,32,33] and where strong precipitation gradients are observed [34]—intense cores of total annual precipitation are observed. High values are also found along the northeastern and northwestern coasts of SA, as well as in the extreme south of Chile. Intermediate annual totals (500–2500 mm/year) are observed in central and southeastern SA, including Northeastern Argentina, Uruguay, and Southeastern Brazil.

The annual and diurnal cycles of precipitation at selected locations in SA (Figure 1C–J) reveal the heterogeneous behavior of this meteorological field, influenced by distinct precipitation regimes and the large spatial extent of the continent. In the northern region of SA, Lake Maracaibo (Figure 1D) exhibits an annual cycle characteristic of a Northern Hemisphere monsoon regime [29], with maxima between August and November and lower values from December to April. The diurnal cycle in Lake Maracaibo (Figure 1D) is

marked by early morning peaks, associated with intense convection and strong electrical activity [35]. On the northwestern coast of SA, in Colombia (Figure 1G), precipitation occurs almost uniformly throughout the year, generally exceeding 500 mm per month. The diurnal cycle at this location features preferential peaks between nighttime and early morning, although notable precipitation rates also occur in the afternoon. In Uruguay (Figure 1F), a relatively uniform annual cycle is observed, with monthly values around 200 mm. The diurnal cycle is poorly defined, with no preferred time for precipitation peaks. Other locations (Figure 1A,E,G–J), situated in the tropical region of South America, are influenced by a monsoon regime typical of the continent. These regions experience peak precipitation between November and March. However, significant differences are observed in both monthly totals and the diurnal cycle, reflecting the influence of diverse systems and physical processes responsible for precipitation formation [8].

2.2. Data

Twenty years of data from the Integrated Multi-satellite Retrievals for the Global Precipitation Measurement (GPM) research product (IMERG, [36,37]) from 2001 to 2020 are used to obtain a consistent characterization of the diurnal cycle of precipitation in SA. This period represents the longest continuous time span available with homogeneous data of high spatial and temporal resolution, which is essential for robust analyses of the variability and trends of the diurnal cycle of precipitation over the last two decades in SA. The Version 06 of the IMERG Final Run Half Hourly $0.1^\circ \times 0.1^\circ$ V06B product (hereafter IMERG, [36]) that estimates the precipitation rate at a high spatial ($0.1^\circ \times 0.1^\circ$) and temporal (30 min) resolution is used. Past studies have found some shortcomings of the IMERG product, e.g., overestimation of drizzle and underestimation of convective precipitation [22], underestimation in mountainous regions and underperformance in coastal regions [23–25]. Despite its limitations—associated with the combination of multiple sensors (e.g., infrared and passive microwave) from different satellites and their inability to detect orographically forced and warm-rain processes [23], as well as issues related to cirrus cloud contamination—IMERG has proven to be a suitable product for studying the diurnal cycle of precipitation at both regional and global scales [11,12,21,38]. In SA, previous studies have demonstrated its ability to capture the diurnal characteristics of precipitation in the tropical region [8,23,25,39], as well as to reproduce the main features of mesoscale convective systems (MCSs, [40,41]), which are the primary precipitation-contributing systems [42] on diurnal timescales. Therefore, the IMERG dataset has been shown to provide reliable estimates of precipitation at high spatial and temporal resolutions, making it particularly suitable for analyzing the variability of the diurnal cycle of precipitation in SA.

2.3. Climatology of the Diurnal Cycle of Precipitation

To calculate the seasonal climatology of the diurnal cycle of precipitation for SA, we follow the methodology used in [8]. Thus, the IMERG dataset is divided into four seasonal periods: December–January–February (DJF), March–April–May (MAM), June–July–August (JJA) and September–October–November (SON). This division is made to maintain consistency with previous studies and to allow comparisons on a continental scale. Then, the precipitation rate composites (Equation (1)) are calculated every 30 min for the four seasonal periods using the following equation:

$$P(\varphi, \lambda, t_{UTC}) = \frac{\sum_{i=1}^{N} P_i(\varphi, \lambda, t_{UTC})}{N} \quad (1)$$

and in Equation (1), N represents the length of the number of days of each seasonal period, and P_i corresponds to the precipitation rate for a specific latitude (φ), longitude (λ), and

UTC time. The final result of Equation (1) is 48 observations ($n = 48$) with half-hourly time steps ($\Delta t = 30$ min) of precipitation rate $P(\varphi, \lambda, t_{UTC})$ representing the diurnal cycle starting at 0000 UTC (Supplementary Video S1).

The diurnal cycle of precipitation for each pixel in the SA region is determined using harmonic analysis, following the approach described in [43]. The two first harmonics are used in this study to represent the variability of the diurnal cycle of precipitation in SA since they depict daily (24 h) and semi-daily (12 h) scale processes. The harmonic function $F(t)$ is represented by Equation (2):

$$F(t) = f_0 + \sum_{k=1}^{2} C_k \cos\left(\frac{2\pi tk}{n} - \phi_k\right) \quad (2)$$

where $F(t)$ represents the precipitation rate at time t (in UTC) for a given latitude (φ) and longitude (λ), f_0 is the mean, n is the sample length, and C_k and ϕ_k represent the amplitude and phase of the k-th order harmonics, respectively. To obtain the amplitude of the harmonic of order k, we use Equation (3) based on the coefficients of the cosine (A_k, Equation (4)) and sine (B_k, and Equation (5)) functions:

$$C_k = [A_k^2 + B_k^2]^{0.5} \quad (3)$$

$$A_k = \frac{2}{n} \sum_{t=1}^{n} Y_t \cos\left(\frac{2\pi tk}{n}\right) \quad (4)$$

$$B_k = \frac{2}{n} \sum_{t=1}^{n} Y_t \sin\left(\frac{2\pi tk}{n}\right) \quad (5)$$

The phase (ϕ_k) of the harmonics of order k is calculated by Equation (6a–c):

$$\phi_k = \arctan\left(\frac{B_k}{A_k}\right), \quad \text{if } A_k > 0 \quad (6a)$$

$$\phi_k = \arctan\left(\frac{B_k}{A_k}\right) \pm \pi, \quad \text{if } A_k < 0 \quad (6b)$$

$$\phi_k = \frac{\pi}{2}, \quad \text{if } A_k = 0 \quad (6c)$$

To determine the time of occurrence of the precipitation rate peaks (Equation (7)), the property of the cosine function is used, which states that its maximum value is reached when its argument equals zero:

$$t_{UTC} = \frac{\phi n}{2\pi k} \quad (7)$$

For comparison with other studies, all UTC times are converted to local solar time (LST, Equation (8)):

$$t_{LST} = t_{UTC} + \frac{\lambda(^\circ)}{15(^\circ h^{-1})} \quad (8)$$

To determine whether each pixel exhibits a single hour (unimodal distribution), two distinct or no clear hour (bimodal or uniform distribution) for the occurrence of the maximum precipitation rate, the normalized amplitude (A_N, Equation (9)) is calculated. According to [44], if the A_N of the first harmonic (1° H) is less than 0.5, the shape of the diurnal distribution will be bimodal or uniform (indicating two peaks or no clear peak, Figure 2A). Conversely, if the A_N of the 1° H is greater than or equal to 0.5, the shape of the diurnal distribution will be unimodal (indicating a single peak, Figure 2B).

$$A_N = \frac{C_k}{f_0} \quad (9)$$

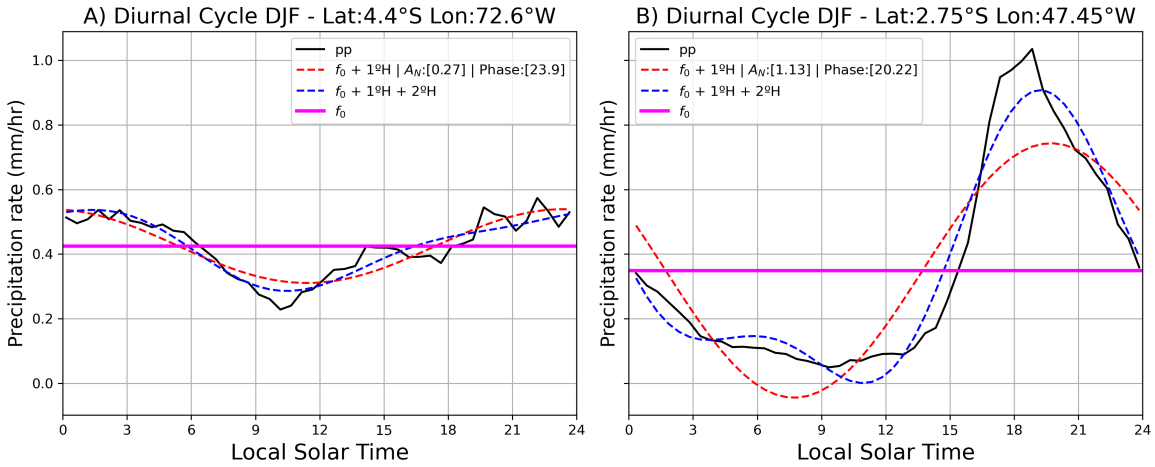


Figure 2. Criteria for the shape of the diurnal distribution of precipitation according to [44]. (**A**) $A_N < 0.5$: bimodal distribution. (**B**) $A_N > 0.5$: unimodal distribution. In both figures, the black curve represents the mean diurnal cycle of precipitation during the DJF period, the magenta curve represents the mean precipitation rate f_0, the red curve represents $f_0 + 1°$ Harmonic (H), and the blue curve represents $f_0 + 1°$ H + 2° H.

2.4. Identification of Homogeneous Regions

Homogeneous regions are defined based on diurnal metrics (mean hourly precipitation rate, normalized amplitude, and phase of the first two harmonics) obtained from the characterization of the diurnal cycle using harmonic analysis. Diurnal metrics have the characteristic of condensing large amounts of data into summary statistics, allowing the diurnal cycle of precipitation to be quantified [11]. To differentiate pixels with unimodal or bimodal/uniform diurnal distributions, a new label named "shape" is created. This label assigns a value of 0 to bimodal/uniform distributions and 1 to unimodal distributions. Then, the diurnal metrics are normalized by dividing by the maximum value of each metric. For dimensionality reduction, the empirical orthogonal function (EOF) technique [45] is applied to the diurnal metrics. According to [46], dimensionality reduction involves converting high-dimensional data (diurnal metrics and shape) into a new lower-dimensional representation (in this work, the first three principal components are used) that retains its essential information and meaning.

The K-Means method [43] is used to identify homogeneous regions, i.e., regions with a similar diurnal cycle of precipitation as a function of diurnal metrics. As a first step before running the K-Means algorithm, it is necessary to determine the number of centroids (clusters). To do this, the elbow method is applied by calculating the sum of squared error (SSE) and the silhouette scores (see Figure A1). The K-Means technique begins by randomly initializing the previously determined centroids. Then, each element of a given cluster is assigned to its nearest centroid (a process called expectation). The average of all elements in each cluster is calculated, and a new centroid is assigned to each cluster (a process called maximization). Finally, the algorithm iterates through the expectation–maximization process until the centroids converge (i.e., until their positions remain the same as in the previous iteration). In this work, we use the Euclidean distance [43] as the dissimilarity measure.

2.5. Trends in the Diurnal Cycle of Precipitation

Since the IMERG product estimates the precipitation rate every 30 min, each pixel presents a total of 48 observations per day. Thus, each pixel in a 20-year observation would have a total of 350,640 measurements. To condense the daily data (48 observations), we

apply harmonic analysis to each day and extract the mean hourly precipitation rate (f_0), the amplitude (C_1), and the normalized amplitude of the first harmonic (A_N). In this way, we create a new daily dataset with the diurnal metrics (see Figure A2), f_0, C_1 and A_N, which quantify the diurnal cycle in terms of its hourly mean intensity, the amplitude of the 24 h oscillation, and the shape of the distribution.

To determine whether the diurnal cycle of precipitation (as a function of f_0, C_1 and A_N) in SA exhibits trends during the period 2001–2020, and to evaluate their statistical significance at the 95% confidence level, the nonparametric Mann–Kendall test [47,48] is applied. Trends in the diurnal cycle in SA are quantified using Sen's slope method [49], a nonparametric technique for estimating the magnitude of trends.

Figure 3 presents a schematic diagram of the methodology employed in this study, covering all stages from data collection to the analysis and discussion of the key highlights.

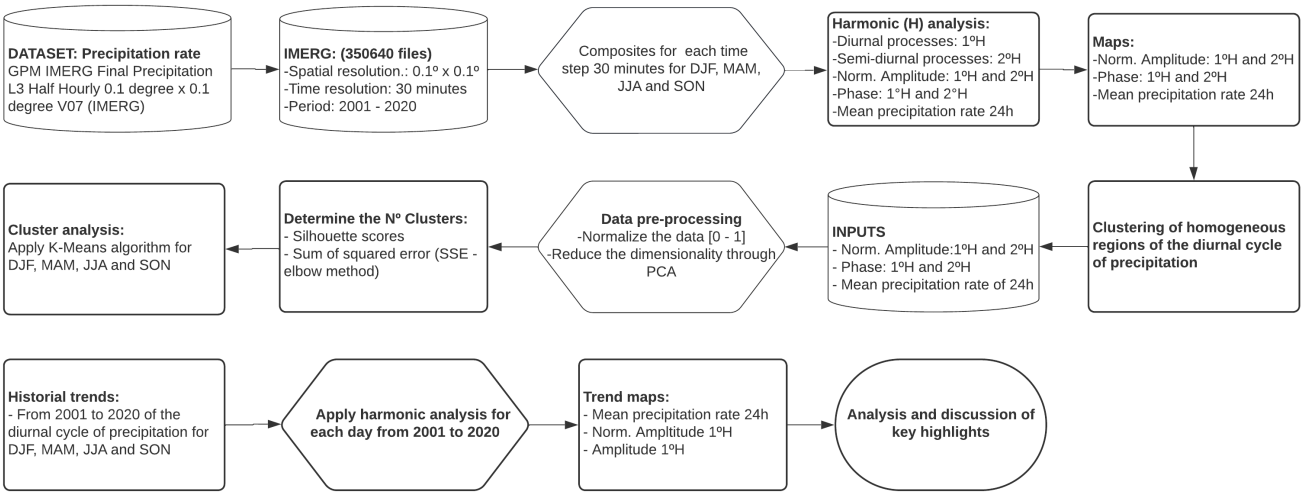


Figure 3. Schematic diagram of the methodology employed in this study, covering all stages from data collection to the analysis and discussion of the key highlights.

3. Results

3.1. Climatology of the Diurnal Cycle of Precipitation

The climatology of the diurnal cycle of precipitation over the whole of South America (SA) and a portion of the surrounding oceans is presented using diurnal metrics: the hourly mean precipitation rate (f_0, Figure 4), the normalized amplitude (A_N, Figure 5) and the phase (ϕ, in LST, Figure 6) of the first harmonic (1° H).

For the hourly mean precipitation rate (f_0, Figure 4), a threshold of 0.254 mm/h (shades of green) is used to associate it with precipitation produced by Mesoscale Convective Systems (MCSs), as in [8,41]. Thus, grid boxes shaded in green indicate areas affected by MCSs, either as their formation regions or as areas influenced by their trajectories. At first glance, the precipitation rate associated with MCSs exhibits seasonality in the tropical and subtropical regions of SA. During the austral spring (SON, Figure 4D), the MCSs-associated precipitation rate (above 0.254 mm/h) is concentrated in the northwestern part of the continent (on the eastern side of the Andes) and extends into southeastern SA (SESA). In the austral summer (DJF, Figure 4A), the precipitation rate exceeding 0.254 mm/h is distributed across much of tropical and subtropical SA, except for the far northern and northeasternmost regions of the continent. During the austral autumn (MAM, Figure 4B), subtropical SA (between 30° S–20° S) experiences a decrease in precipitation rate intensity associated with MCSs, along with a noticeable shift of values exceeding 0.254 mm/h toward the equator. In the austral winter (JJA, Figure 4C), precipitation rates exceeding 0.254 mm/h

are primarily concentrated in the northern region of SA, with highest values occurring north of the equator. Another important point to highlight is the existence of regions where precipitation rates exceed 0.254 mm/h throughout the year. These regions include the extreme south of the continent, SESA (Southern Brazil, Uruguay and Northeastern Argentina), the coastal region of Colombia, and the northwestern of the Amazon Basin. Furthermore, throughout the Andes, there is evidence of regions that are favorable for the year-round occurrence of MCSs, such as precipitation hotspots [5,32,33] located on the eastern side of the Andes at around 1500 m altitude over Peru (in the Central Andes and Cusco) and Bolivia (Santa Cruz).

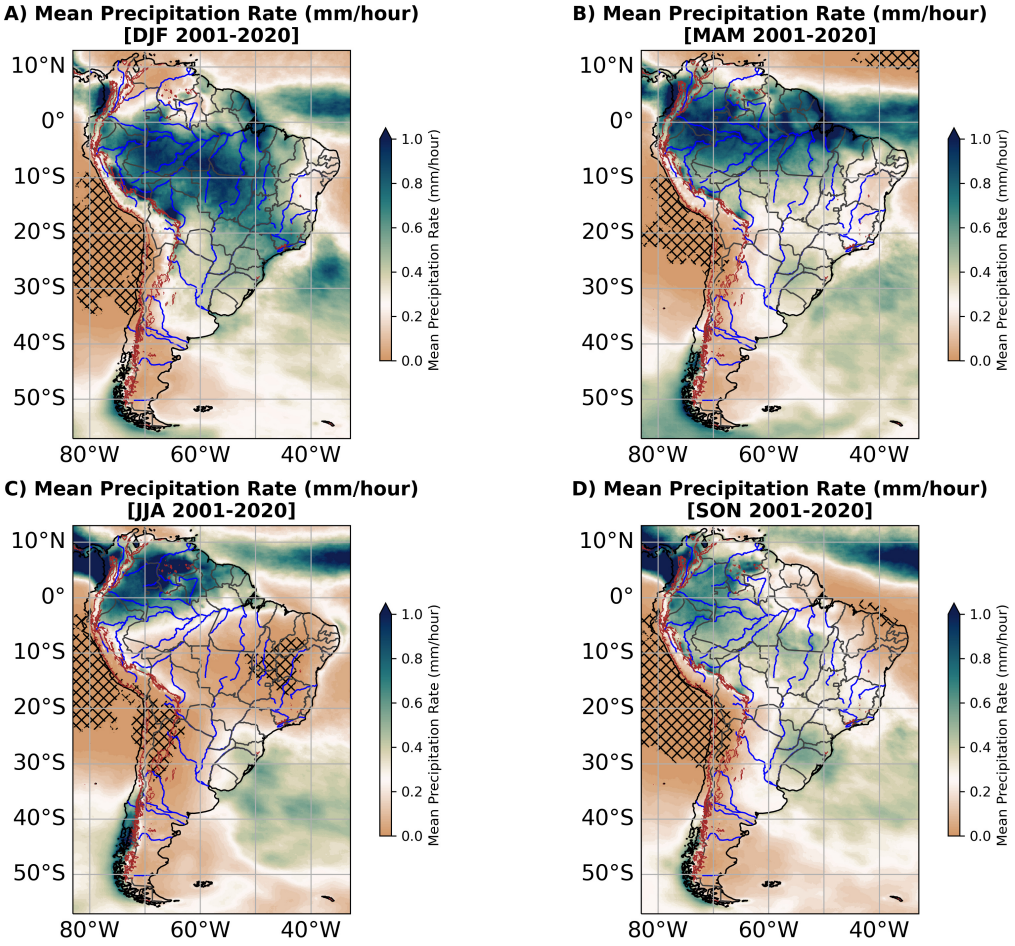


Figure 4. Intensity of the hourly average precipitation rate (f_0) (mm/h). (**A**) December–January–February (DJF). (**B**) March–April–May (MAM). (**C**) June–July–August (JJA). (**D**) September–October–November (SON). The blue lines depict the main rivers of South America (SA). The brown lines extending from the extreme south to the extreme north of SA mark the 1500 m a.s.l. elevation of the Andes and other highland regions. Pixels with intensities below 0.01 mm/h are marked with crosses ("xx") and represent regions with scarce precipitation. Values exceeding 0.254 mm/h are represented by a gradient of green shades.

Over the oceans near the continent, regions with precipitation rates greater than 0.254 mm/h can be observed throughout the year. These regions are the southern tip of the Pacific Ocean near the continent, the subtropical Atlantic Ocean, and in the equatorial zone of the Pacific and Atlantic Oceans, indicating the climatological location of the Inter-Tropical Convergence Zone (ITZC).

The normalized amplitude of the first harmonic (A_N, Figure 5) indicates the regions where the diurnal distribution of precipitation rate as a function of time of day follows ei-

ther a bimodal/uniform pattern ($A_N < 0.5$) or a unimodal pattern ($A_N > 0.5$). Bimodal (or uniform) diurnal distributions represent grid cells where precipitation rate exhibits two predominant peak times (or lacks a well-defined peak). On the other hand, unimodal diurnal distributions indicate grid cells where the precipitation rate exhibits a single predominant peak time. Figure 6 shows the predominant times of occurrence of precipitation rate peaks (phase of the first harmonic, ϕ). In this study, we divide the day into four periods: early morning (00–06 LST), morning (06–12 LST), afternoon (12–18 LST), and evening (18–24 LST). Thus, tropical coastal areas and regions extending a few hundred kilometers inland exhibit unimodal diurnal distributions throughout the year (Figure 5), with precipitation rate peaks occurring between mid-afternoon and early evening (15–21 LST, Figure 6). Over the Amazon Basin (AB), a northwest–southeast extension zone of grid cells exhibits bimodal distributions, mainly during the DJF (Figure 5A) and MAM (Figure 5B) periods. This zone exhibits peak precipitation rate occurrences during early morning, morning, afternoon, and evening hours. The progression of these peaks follows an east–west direction from the eastern side of SA and a west–east direction from the western side of the AB (Figure 6). The SESA (including Southeastern Brazil, Uruguay, and Northeastern Argentina) is characterized by a bimodal or uniform distribution (Figure 5), with precipitation rate peaks occurring between early morning and morning (03–09 LST, Figure 6) throughout the year. Along the Andean range (above 1500 masl), mainly in tropical and subtropical latitudes, diurnal distributions are unimodal (Figure 5) with precipitation rate peaks occurring in the afternoon and early evening (15–21 LST, Figure 6) throughout the year. South of 25° S to the southern tip of SA, the diurnal distribution is predominantly bimodal or uniform (Figure 5), except in a region near 1500 msal, where $A_N > 0.5$ and precipitation rate peaks occur at night (Figure 6). In this region, the timing of occurrence of precipitation rate peaks shows a noisy signal (Figure 6). This area is characterized by a weak diurnal cycle and the the influence of high-frequency transient systems moving from west to east (from the Pacific Ocean to the Atlantic Ocean).

Over the Atlantic Ocean, a unimodal behavior (Figure 5) is observed only in areas closest to the coast, with precipitation rate peaks occurring between late night and early morning hours (21–03 LST, Figure 6). As one moves away from the oceanic region closer to the coast, the precipitation rate behavior becomes bimodal (Figure 5), with peaks occurring between the early morning and morning hours (Figure 6). Over the Pacific Ocean, the diurnal cycle exhibits a strong signal and a unimodal distribution (Figure 5), mainly north of the Equator (off the coast of Colombia), with peaks occurring in the morning hours (06–12 LST, Figure 6). Between 10° S and 30° S, the diurnal cycle is weak, with few or no precipitation events (precipitation rate < 0.01 mm/h, Figure 4). These regions are represented in the diurnal metrics figures with crosses (“xx”). Continental regions with scarce precipitation events (precipitation rate < 0.01 mm/h) are marked with crosses (“xx") and are mainly observed during the JJA period. In mid-latitudes, the Pacific Ocean exhibits a weak diurnal cycle and a bimodal diurnal distribution, with a noisy signal in the timing of peak occurrence (Figure 6). This noisy phase signal highlights the influence of high-frequency transient systems propagating west to east across this region, with the noise persisting over the southernmost Atlantic.

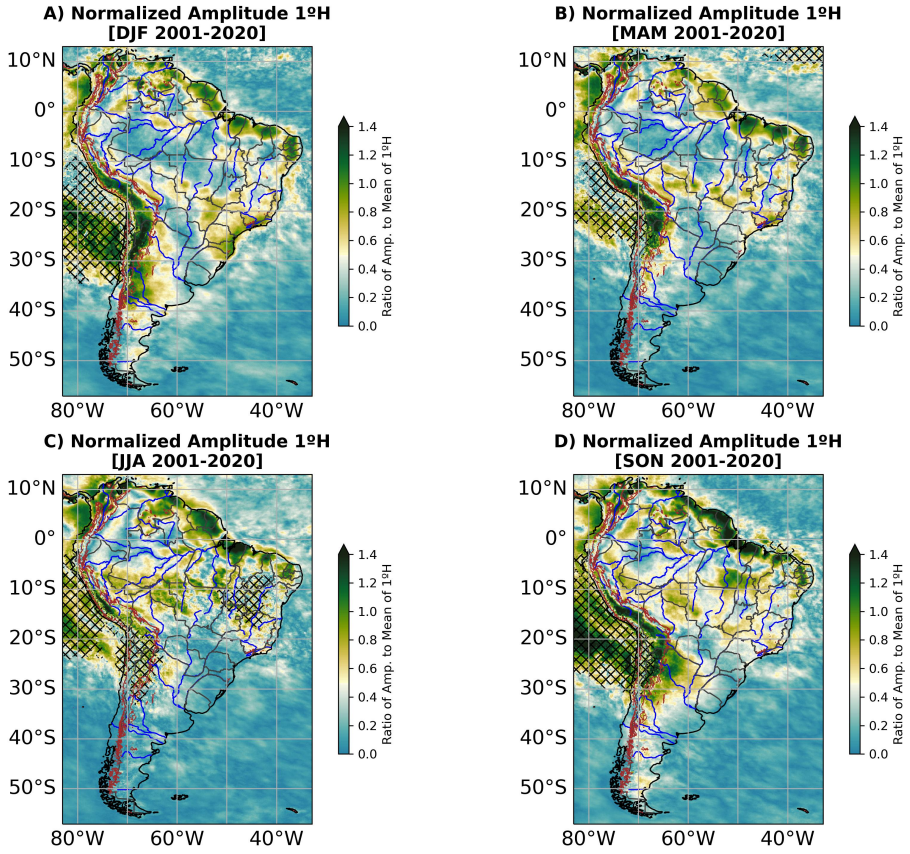


Figure 5. Shape of the diurnal distribution of the precipitation rate (mm/h) through the normalized amplitude (A_N) of the 1° H. (**A**) December–January–February (DJF). (**B**) March–April–May (MAM). (**C**) June–July–August (JJA). (**D**) September–October–November (SON). The blue lines depict the main rivers of South America (SA). The brown lines extending from the extreme south to the extreme north of SA mark the 1500 m a.s.l. elevation of the Andes and other highlands regions. Pixels with intensities below 0.01 mm/h are marked with crosses ("xx") and represent regions with scarce precipitation.

3.2. Regions with a Homogeneous Diurnal Cycle of Precipitation

The regions with homogeneous diurnal cycles of precipitation (grid cells grouped within a cluster labeled with a specific number) in SA, defined based on diurnal metrics (f_0, $A_{N_{1,2}}$, and $\phi_{1,2}$) for the four periods of the year, are shown in Figure 7. The grid cells marked with "+" symbols exhibit diurnal distributions of the bimodal or uniform type to facilitate the differentiation between clusters with bimodal or uniform behavior and those with unimodal behavior (which do not have "+" symbols). At first glance, it is observed that the austral summer, autumn, and winter periods exhibit eight clusters (Figure 7A–C), except for the austral spring, which exhibits nine clusters (Figure 7D). At tropical and subtropical latitudes of SA, the spatial distribution of the clusters follows the seasonal behavior of the mean hourly precipitation rate, varying according to the period of the year. At mid-latitudes, the spatial configuration of the clusters tends to be more constant; however, small differences are observed between periods, likely due to the seasonality of transient systems frequency. The areas shaded in black indicate precipitation rates below 0.01 mm/h, representing arid regions or regions with scarce precipitation events.

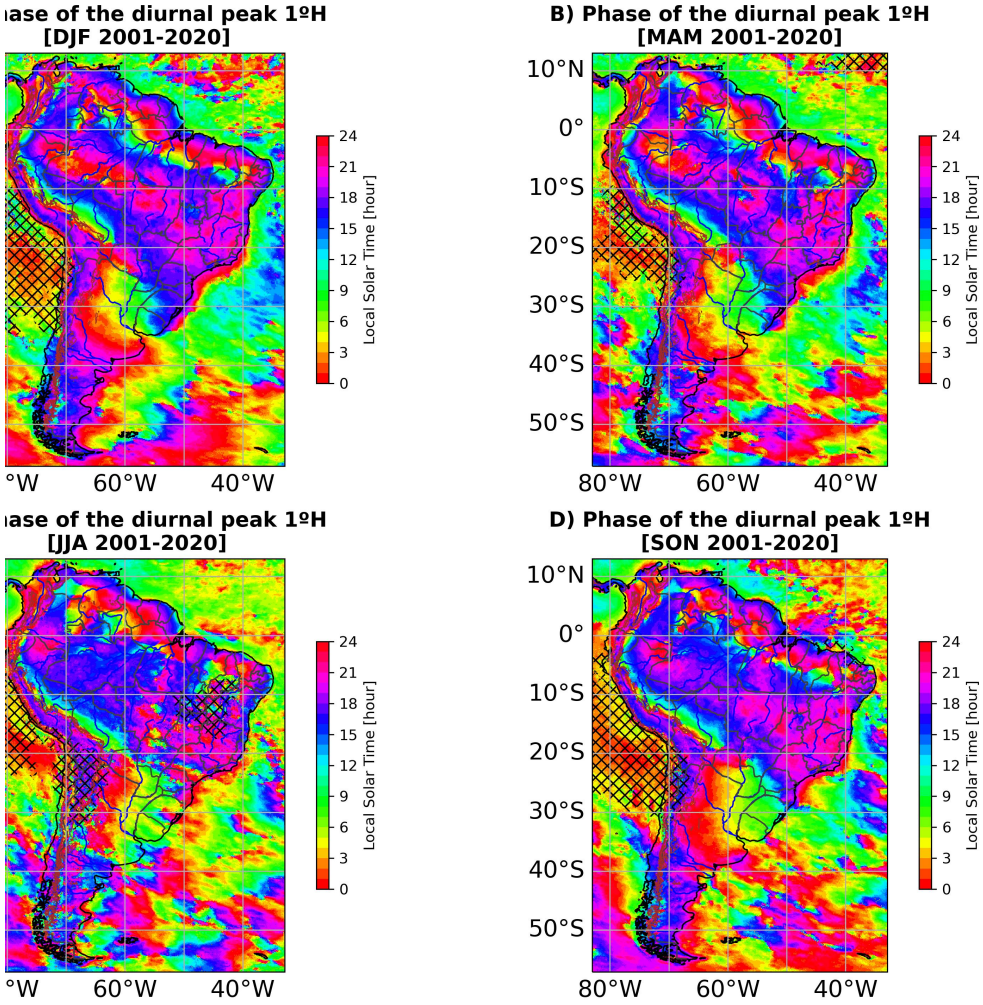


Figure 6. Timing of occurrence of the maxima (Local Solar Time, LST) of the diurnal-scale processes through the phase (ϕ) of the 1° H. (**A**) December–January–February (DJF). (**B**) March–April–May (MAM). (**C**) June–July–August (JJA). (**D**) September–October–November (SON). The blue lines depict the main rivers of South America (SA). The brown lines extending from the extreme south to the extreme north of SA mark the 1500 m a.s.l. elevation of the Andes and other highlands regions. Pixels with intensities below 0.01 mm/h are marked with crosses ("xx") and represent regions with scarce precipitation.

Table 1 presents a summary of the main characteristics of the clusters identified at each station: mean hourly precipitation rate f_0, normalized amplitude (A_N), the phase (ϕ) of the 1° H, and their geographic locations. In the austral summer (DJF, Figure 7A), all clusters (except for the northernmost part of South America, Northeastern Brazil, the western coasts of Chile and Peru, and the mid-latitudes of Argentina) are influenced by the occurrence of MCSs, defined as having precipitation rates greater than 0.254 mm/h [41]. Half of the clusters (2, 4, 6, and 7) exhibit DCPs with bimodal behavior, characterized by a more intense peak between night and morning hours, and a secondary peak from morning to afternoon. Clusters 1, 3, 5, and 8 display unimodal behavior, with peaks occurring predominantly between evening and night. Cluster 1 is noteworthy for presenting peaks during the morning hours and is located in the eastern sector of the Central Andes, encompassing the precipitation hotspot regions of Peru and Bolivia [5,32,33], an area characterized by strong precipitation gradients [34]. Cluster 5 also stands out due to its exposure to intense precipitation rates associated with squall lines (SLs) induced by sea breezes [50,51] along the Atlantic coast. In addition, cluster 5

is also affected by MCSs near the coasts of Ecuador and Colombia. For more details on the geographic distribution of each cluster, refer to Table 1.

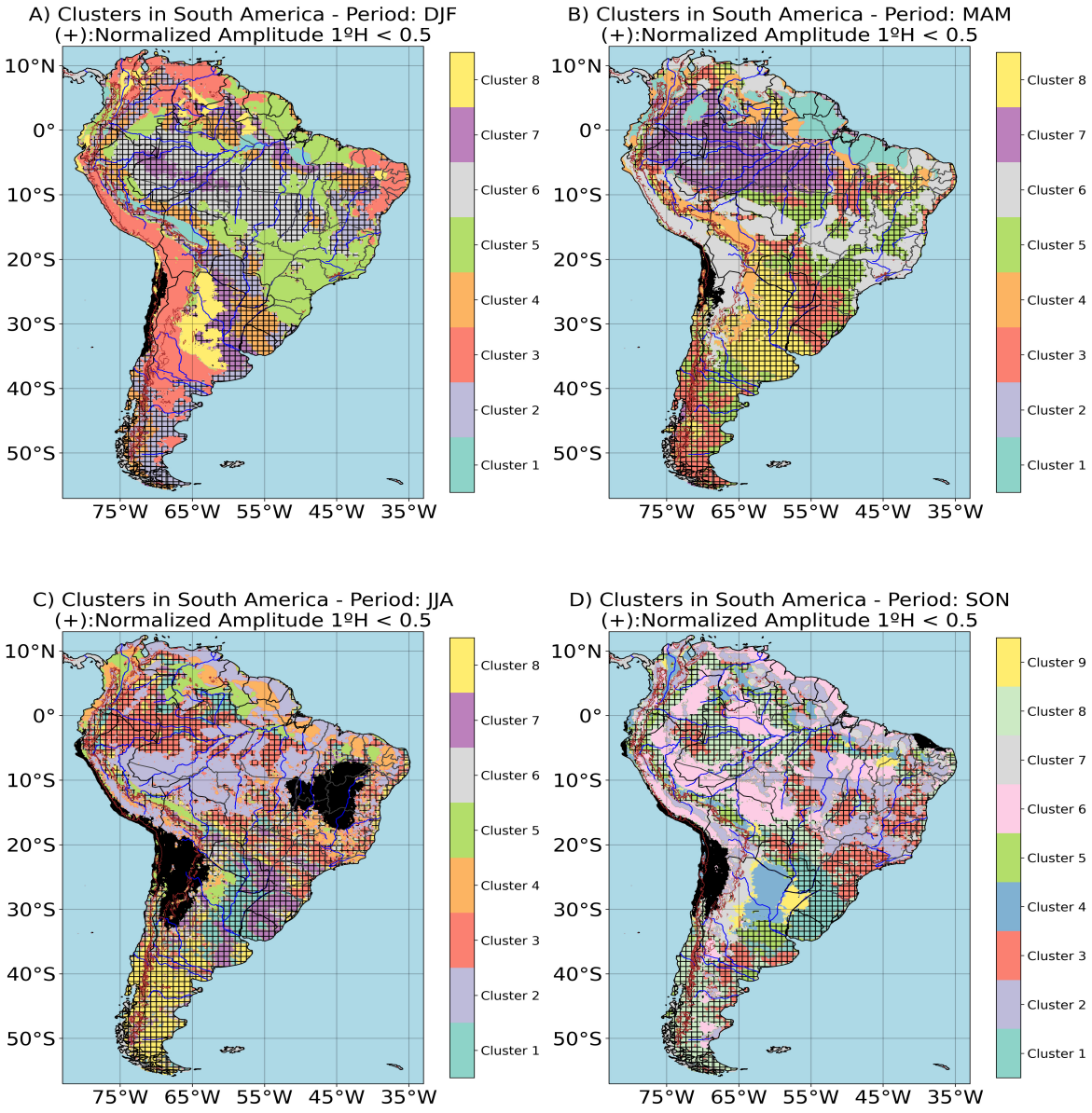


Figure 7. Clustering of regions with homogeneous diurnal cycles of precipitation in South America (SA). (**A**) December–January–February (DJF). (**B**) March–April–May (MAM). (**C**) June–July–August (JJA). (**D**) September–October–November (SON). Black crosses "++" indicate grid boxes with an $A_N < 0.5$. The blue lines depict the main rivers of SA. The brown lines extending from the extreme south to the extreme north of SA mark the 1500 m a.s.l. elevation of the Andes and other highlands regions. Black grid boxes represent regions with scarce precipitation (precipitation rate < 0.01 mm/h).

Table 1. Clusters identified across SA for each season: December–February (DJF), March–May (MAM), June–August (JJA), and September–November (SON). A_N and ϕ refer to the normalized amplitude and the phase of the first harmonic, respectively. The acronyms denote geographic directions: E (East), N (North), S (South), W (West), SE (Southeast), NE (Northeast), NW (Northwest), and SW (Southwest). The letters "B" and "U" in the A_N column indicate bimodal and unimodal diurnal distributions, respectively.

Season	Cluster	Precipitation Rate (mm/h)	A_N	Phase (ϕ)	Geographic Location
DJF	1	>0.254	>0.5 (U)	morning	Hotspots regions of Peru and Bolivia; eastern side of the central Andes in Peru; Amazon region of Ecuador; coast of Colombia; and Amazonian rivers in Brazil.
	2	≈0.254	<0.5 (B)	late afternoon–evening	Paraguay; SE of Brazil; Southern Argentina; NW of SA (Ecuador, Colombia and Venezuela).
	3	<0.254	>0.5 (U)	afternoon–night	Northeasternmost region, extreme north, Western region of SA (Argentina, Bolivia, Chile and Peru).
	4	≈0.4	<0.5 (B)	afternoon, dawn	SE of SA (NE of Argentina, SE of Brazil and Uruguay); NE of Bolivia; Peruvian, Ecuadorian and Colombian Amazon; northern and Northeastern Brazil; Southern Argentina and Chile.
	5	>0.254	>0.5 (U)	afternoon–night	NE-SA; SE-Brazil; coastal region of Colombia; some inland regions.
	6	>0.254	<0.5 (B)	night–dawn, afternoon	Tropical region of SA (in the AB) with a northwest-southeast-oriented configuration.
	7	>0.254	<0.5 (B)	night–dawn, afternoon	Tropical region of SA (inside the AB) with a northwest-southeast-oriented configuration; NE Argentina.
	8	≈0.254	>0.5 (U)	nightime	Argentina; Ecuador; NE and N of Brazil; Southern Guyana; Venezuela; highland of Colombia; and northern Peru.
MAM	1	>0.254	>0.5 (U)	afternoon–evening	Along the western and eastern coasts of SA
	2	≈0.6	<0.5 (B)	early morning, afternoon	AB (north of 10° S).
	3	0.4 mm/h; <0.254 (S. Argentina)	<0.5 (B)	afternoon–evening, morning	Northern Uruguay; Southern, Western Center and Northeastern Brazil; Southern Chile and Argentina; Venezuela; and northern highlands of Peru.
	4	≈0.4	>0.5 (U)	dawn–morning	In region with altitudes ranging from 600 to 1500 masl; hotspot regions of Peru and Bolivia and area of intense precipitation gradient located along the eastern slopes of the Central Andes in Peru.

Table 1. *Cont.*

Season	Cluster	Precipitation Rate (mm/h)	A_N	Phase (ϕ)	Geographic Location
MAM	5	≈0.254	<0.5 (B)	afternoon–evening, morning	Highland of Ecuador and Peru; Southern and Central Argentina; Southern and Central Chile; Southern, Northeastern, and Western Center Brazil; and some regions in the extreme north of SA.
	6	<0.254	>0.5 (U)	afternoon–evening	Along the western and eastern coasts of SA.
	7	≈0.6	<0.5 (B)	afternoon–evening, early morning	AB (north of 10 S); southernmost of SA (Southern Chile).
	8	≈0.4	<0.5 (B)	early morning–morning, late afternoon	SE of SA (Northern and Northeastern Argentina, Southern Uruguay); Paraguay; Bolivia; Peru; Southern Argentina; North and Northeastern Brazil; Venezuela.
JJA	1	<0.254	<0.5 (B)	early morning–morning, afternoon	Subtropical region and mid-latitudes (Argentina).
	2	>0.254 (N. equator); <0.254 (S. equator)	>0.5 (U)	afternoon	Tropical region of SA (near 10 S—including highest elevations of the tropical Andes in Bolivia and Peru, coastal region on the eastern side of SA).
	3	>0.6 (north of 5 °S); <0.254 (south of 5 °S)	<0.5 (B)	afternoon–evening, early morning–morning	Brazilian, Colombian, Ecuadorian, and Peruvian Amazon; parts of Venezuela; some regions of Southeastern Brazil.
	4	>0.6 (N. equator); <0.254 (S. equator)	>0.5 (U)	nighttime–dawn	Tropical region of SA (along the coastal regions of Colombia and Ecuador, over tropical Andes of Bolivia and Peru–above 1500 masl—, and a few hundred kilometers inland from the coast in the northern and northeastern regions of SA).
	5	>0.8 (N. equator); <0.254 (S. equator)	>0.5 (U)	late dawn–morning	Tropical region of SA (Colombia, some regions in Ecuador, Bolivia and Peru—covering precipitation hotspots below 1500 masl); Northern Argentina; a few kilometers inland from the eastern coast of SA.
	6	<0.254	<0.5 (B)	morning, evening	Southeastern Brazil; Paraguay; and Southern Argentina.
	7	>0.254	<0.5 (B)	morning, night-to-dawn	Southeastern region of SA (Southeastern Brazil, Uruguay, and Northeastern Argentina); Paraguay.
	8	<0.254	<0.5 (B)	noisy signal	Southern Argentina; Southern Chile.
SON	1	≈0.6	<0.5 (B)	afternoon, morning	SE of SA.

Table 1. *Cont.*

Season	Cluster	Precipitation Rate (mm/h)	A_N	Phase (ϕ)	Geographic Location
SON	2	<0.254 (Andean Mountains and near the eastern coast of SA); >0.254 (along the northern coast of the continent and over the AB)	>0.5 (U)	afternoon–evening	High elevations of the Andean Mountain; a few hundred kilometers inland from the northeastern coast of SA; along the northern coast of the continent; over the AB.
	3	>0.254 (Amazon and SE. Brazil); <0.254 (E. Brazil, and Argentina)	<0.5 (B)	night-to-morning, afternoon	Southeastern and Eastern Brazil; Brazilian and Peruvian Amazon; central region of Argentina.
	4	≈ 0.254 (S. equator); >0.254 (N. equator)	>0.5 (U)	night-to-early morning	Venezuela (near Lake Maracaibo); Colombia near the Andes; Southern Paraguay; Northern Argentina.
	5	>0.254	<0.5 (B)	late dawn–morning, late afternoon–evening	Scattered across several regions of SA (including the precipitation hotspots regions); eastern side of the Central and Northern Andes of Peru; Northeastern Argentina; Ecuador; Colombia; and the Brazilian Amazon.
	6	>0.254 (in the AB); <0.254 (in the others areas)	>0.5 (U)	afternoon	Andean region (above 1500 m a.s.l.) of Bolivia and Peru; along the northern and northeastern coast of SA; in the AB; and some portions of Argentina.
	7	<0.254	>0.5 (U)	night	A few hundred kilometers inland from the northeastern and northern coasts of SA; Ecuador, Colombia; and the mountains region of Northwestern Argentina.
	8	>0.254 (Amazonian regions, Ecuador, Colombia and Venezuela); <0.254 (in the other regions)	<0.5 (B)	afternoon, early morning	Southern Argentina; Central and Southern Chile; Peru (in the northern part of the Andes and its Amazon region); the Brazilian Amazon; and along the northeastern coast of Brazil, Ecuador Colombia and Venezuela.
	9	>0.254 (Northeastern Argentina, and Colombia); <0.254 (in the other regions)	>0.5 (U)	dawn–morning	Northwest (parallel to the Andes configuration) and northeast of Argentina; the interior of Northeastern Brazil; and Colombia.

While in the austral summer, all clusters are influenced by MCSs, during the March to May period (MAM, Figure 7B), clusters 3 (Southern Argentina), 5, and 6, as well as those located along the northern coast and central Chile, exhibit precipitation rates below 0.254 mm/h. In austral autumn, more than half of the clusters (2, 3, 5, 7, and 8) display bimodal behavior, with pronounced peaks occurring during the night-to-early morning period (Figures 6B and A4B), and a secondary peak during the afternoon (Figure A5B). The remaining clusters (1, 4, and 6) exhibit unimodal diurnal precipitation rate distributions, with peaks mainly between the afternoon and evening hours. Cluster 4, which extends from the eastern sector of the Central Andes in Peru to the Andean region of Argentina (approximately 1500 m a.s.l.), shows peak precipitation during the early morning to morning hours. This region is marked by strong precipitation gradients and encompasses the already known precipitation hotspots, although the intensities observed are lower compared to those during the DJF period [5,32,33].

The July–August period (JJA, Figure 7C) is characterized by a noisy spatial distribution of clusters across the mid-latitudes and subtropical regions. This variability is likely associated with the increased frequency of transient systems propagating from the mid-latitudes toward the equator in a southwest–northeast direction. During this period, most clusters exhibit precipitation rates below 0.254 mm/h, with the exception of cluster 7, located in SESA, and clusters situated north of the equator, in Northwestern Peru and extreme Southern Chile (Figure 4C, Table 1). Five clusters (1, 3, 6, 7, and 8) show bimodal behavior, with predominant peaks occurring during the early morning–morning and afternoon–night periods. Cluster 8, however, exhibits a noisy phase signal (Figure 6C). Clusters 2, 4, and 5 exhibit unimodal diurnal distributions, with peak precipitation rate in the afternoon (cluster 2), evening–early morning (cluster 4), and early morning (cluster 5). Once again, the eastern region of the Central Andes in Peru (cluster 5), which encompasses known precipitation hotspots (Cusco, Peru; and Santa Cruz, Bolivia), stand out due to intense precipitation gradients—albeit being of a lower magnitude compared to other seasons [5,32–34]. In addition, the Western Andes region of Ecuador and Colombia highlight for its high precipitation rates and well-defined unimodal DCP with nocturnal peaks. These are attributed to the interaction between local circulations and large-scale flows [3,19].

The austral spring (SON, Figure 7D), in contrast to the previous periods, is characterized by nine distinct types of diurnal cycles of precipitation across SA. During this period, the spatial configuration of the clusters begins to resemble that observed in the DJF season (Figure 7A). Five clusters (2, 4, 6, 7, and 9) exhibit a unimodal diurnal pattern, with peaks occurring between the afternoon–evening–early morning hours. The remaining four clusters (1, 3, 5, and 8) reveal a bimodal distribution, with peaks typically between the afternoon–evening and early morning–morning periods. Almost all clusters are affected by MCSs, with the exception of cluster 7, and are predominantly located in the AB domain (the northwest–southeast oriented band), SESA, and at the northern and southern extremities of the continent. Notably, during this season, the precipitation hotspot region (cluster 5) exhibits a bimodal diurnal distribution, differing from previous periods. In this case, peaks occur during the early morning and late afternoon–evening (Table 1).

3.3. Trends in the Diurnal Cycle of Precipitation

Historical trends in the DCP over SA are assessed using IMERG product data, based on the mean hourly precipitation rate (f_0), the amplitude (C_1), and the normalized amplitude (A_N) of the first harmonic (Figures 8–10, respectively). Statistically significant trends at the 95% confidence level are primarily concentrated in the tropical region, particularly within the Amazon Basin (AB), and show substantial seasonal variability.

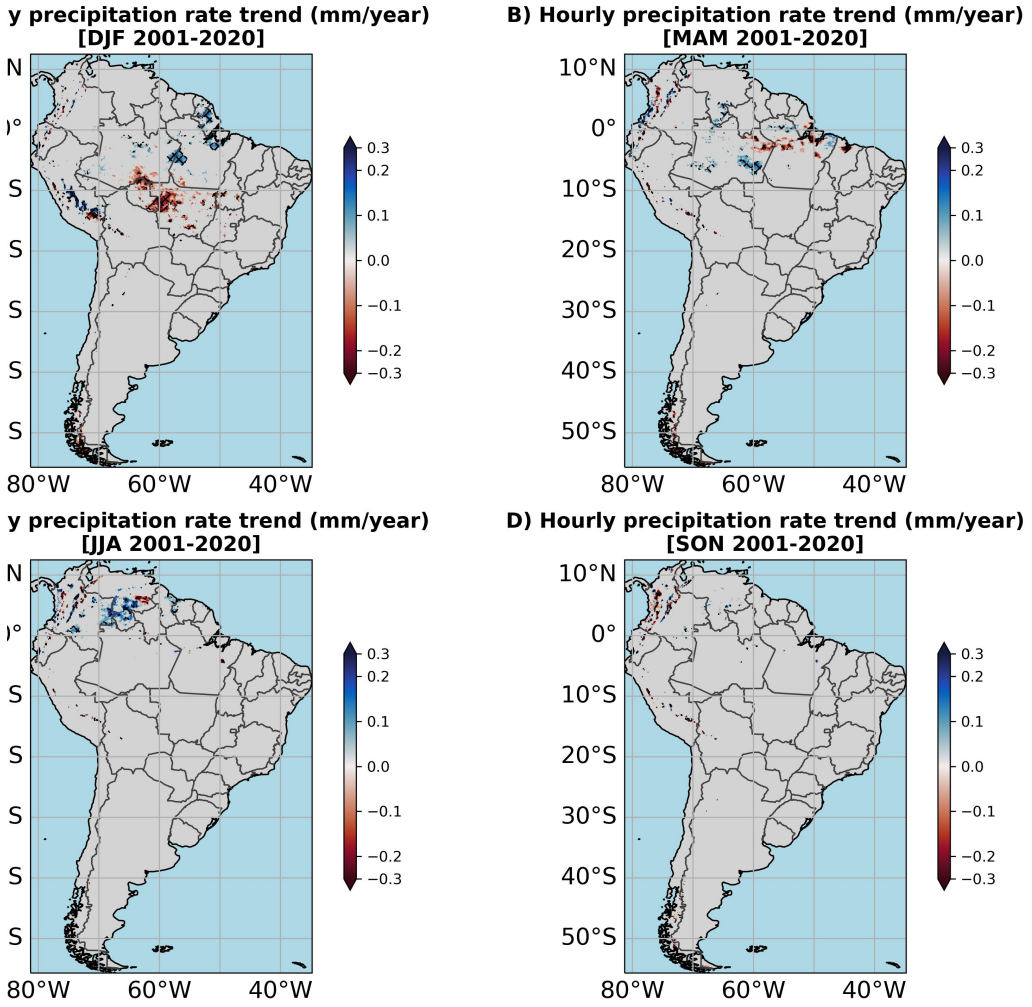


Figure 8. Historical trends of the diurnal cycle of precipitation from 2001 to 2020 of the hourly mean precipitation rate (f_0) in South America. (**A**) December–January–February (DJF). (**B**) March–April–May (MAM). (**C**) June–July–August (JJA). (**D**) September–October–November (SON). Black "x" symbols indicate grid boxes with significant trends at the 95% confidence level.

In DJF, positive trends in f_0 (Figure 8A) and C_1 (Figure 9A) are concentrated in the northeastern region (NESA), encompassing French Guiana and the Brazilian states of Amapá and Pará, along the eastern slopes of the Central Andes, and between Brazilian states of Amazonas and Pará. Decreasing trends were observed in Central–Western Brazil (e.g., Mato Grosso, Rondônia, and Southern Amazonas) and in the Andean region of Southern Peru. During MAM (Figures 8B and 9B), increase trends are observed over the Brazilian states of Amazonas and Pará (northern and northeastern regions), as well as in Venezuela and along the Andean mountains of Colombia, Ecuador, and Peru. Conversely, a decreasing trend in f_0 and C_1 is observed primarily along the Amazonas River, with a greater magnitude and a relatively larger spatial extent in C_1. This decreasing trend is also evident in the state of Maranhão (Brazil), across the Andean regions of Colombia, Ecuador, Venezuela, and Peru, as well as in the extreme south of Chile. In JJA (Figures 8C and 9C), increases occur mainly north of the equator (Venezuela, Colombia). This increase also occurs parallel to the Andean mountain range in Colombia (on both the western and eastern slopes) and Ecuador, while decreases are evident in the Southeastern Venezuela and Andean sectors. During SON (Figures 8D and 9D), the trends are more spatially fragmented, with small positive anomalies interspersed among widespread negative signals in the Andes and Northwestern Amazon.

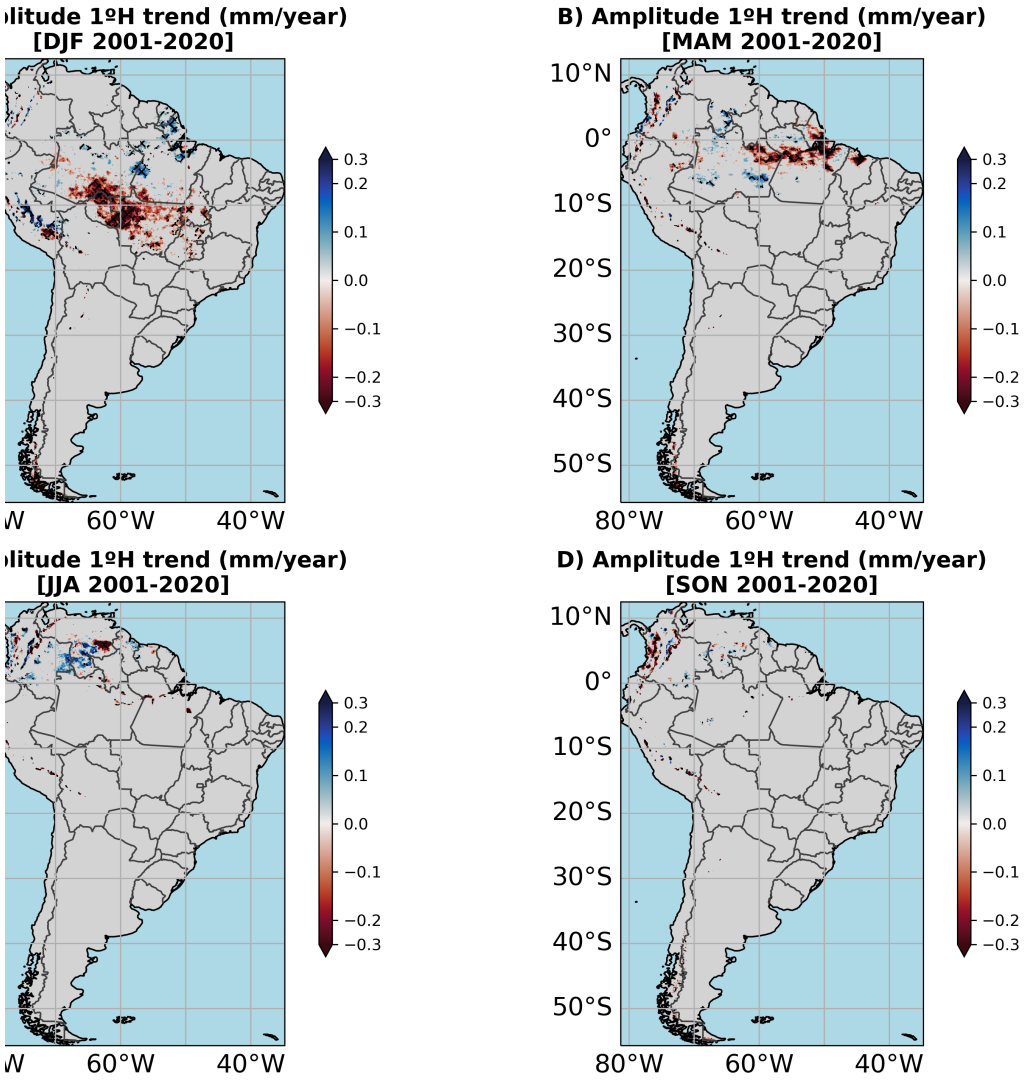


Figure 9. Historical trends of the diurnal cycle of precipitation from 2001 to 2020 of the amplitude of the first harmonic (C_1) in South America. (**A**) December–January–February (DJF). (**B**) March–April–May (MAM). (**C**) June–July–August (JJA). (**D**) September–October–November (SON). Black "x" symbols indicate grid boxes with significant trends at the 95% confidence level.

Trends in the normalized amplitude (A_N, Figure 10), which reflects changes in the shape of the diurnal distribution, are predominantly negative across the AB, particularly along the Amazonas River axis. A seasonal northward migration of these negative trends is observed: central AB in DJF (Figure 10A), northern AB in MAM (Figure 10B) and JJA (Figure 10C), and more dispersed patterns in SON (Figure 10D). This suggests the presence of a bimodal DCP, characterized by two precipitation peaks: one likely associated with nocturnal MCSs, and the other with convective processes driven by surface heating. Limited areas—such as parts of the Andean foothills—show localized increases in A_N, but these were not spatially dominant.

Trends in f_0, C_1, and A_N reveal seasonally dependent and regionally heterogeneous changes in the DCP over tropical SA from 2001 to 2020. Notably, the consistent negative trends in A_N along the Amazonas River may reflect structural shifts in the diurnal distributions. These patterns suggest complex interactions among regional circulation, land–atmosphere feedbacks, and possibly anthropogenic influences affecting the DCP.

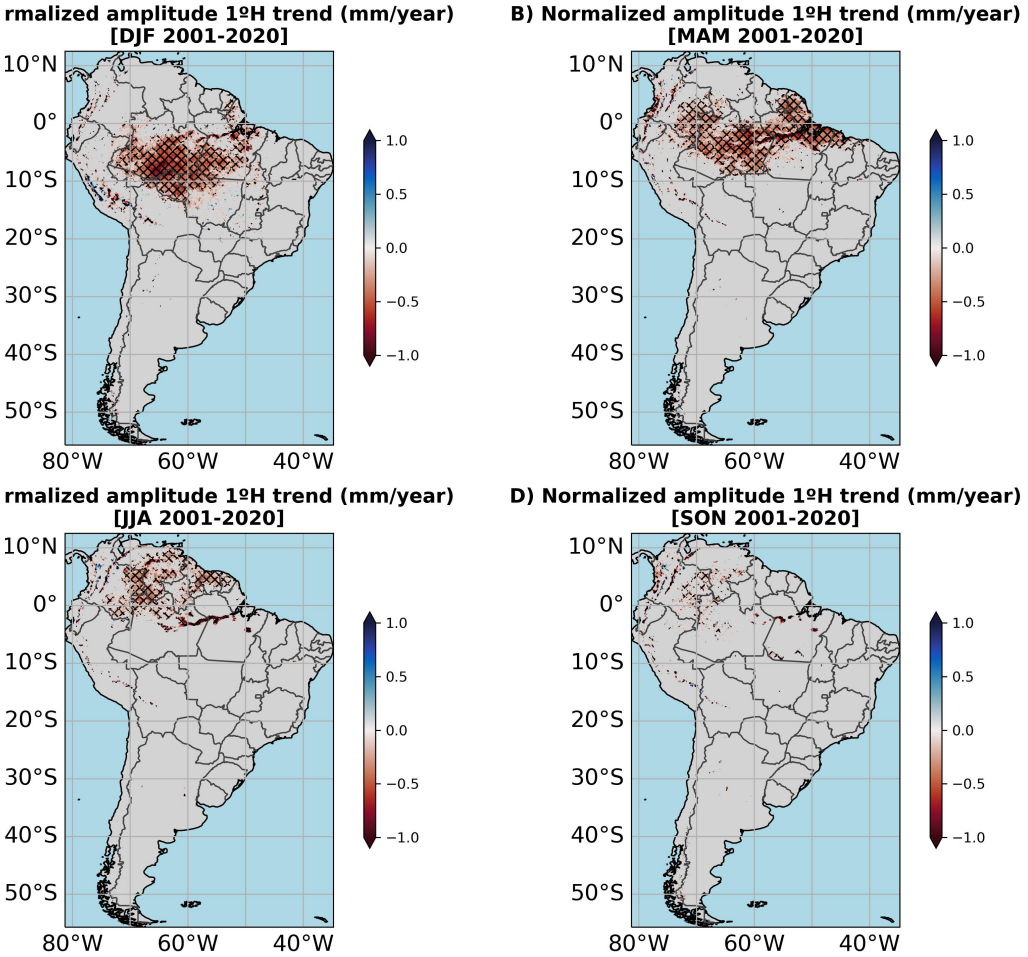


Figure 10. Historical trends of the diurnal cycle of precipitation from 2001 to 2020 of the normalized amplitude of the first harmonic (A_N) in South America. (**A**) December–January–February (DJF). (**B**) March–April–May (MAM). (**C**) June–July–August (JJA). (**D**) September–October–November (SON). Black "x" symbols indicate grid boxes with significant trends at the 95% confidence level.

4. Discussion

4.1. Mean Hourly Precipitation Rate

From f_0 (Figure 4), it is evident that mesoscale convective systems (MCSs, $f_0 > 0.254$ mm/h) are the main systems organizing precipitation in the tropical and subtropical regions of SA [42]. These systems are widely distributed from December to May, undergo a seasonal retreat toward equatorial latitudes during July–August, and subsequently migrate toward the subtropical latitudes of the Southern Hemisphere between September and November. This meridional displacement of MCSs [40] is modulated by deep convection, which is, in turn, driven by solar forcing [52]. Nevertheless, specific regions such as SESA [53–56], the coastal region of northwestern SA (NWSA, in Colombia; [3]), and precipitation hotspots (Eastern Andes of Peru and Bolivia, [5,32,33]) remain active centers of MCS development throughout the year, with consistently high precipitation rates (Figure 1F,G,J, respectively). In SESA and at the locations of precipitation hotspots, the South American Low-Level Jet (SALLJ; [53–55,57,58]) brings residual moisture from the AB, providing a key moisture source that sustains MCS activity. Meanwhile, in the NWSA region, the interaction between large-scale circulation patterns (e.g., between Chocó low-level jet and easterly trade winds, [19,59]) and mesoscale processes favors the persistent initiation of these systems. In these regions of SA, f_0 associated with MCSs indicates that the DCP is strongly modulated by large-scale atmospheric mechanisms and processes,

such as the South American Monsoon System (SAMS, [27–31,40,41,60–62]). Local physical processes (e.g., diurnal cycle of sensible and latent heat fluxes), as well as thermally induced mesoscale circulations modulated by local factors affect MCSs characteristics—including their frequency, life cycle, and intensity [8,60,61]—and therefore the DCP.

Over the tropical Pacific and Atlantic Oceans, the band of intense precipitation rate is associated with the ITCZ [63]. The displacement of the ITCZ throughout the year results from the convergence of the trade winds, reaching its southernmost position during austral summer and its northernmost position during austral winter (see Figure 1 in [64]), affecting the coastal regions near this meteorological system [65,66]. Over the South Pacific and adjacent regions of Chile and Peru, large-scale subsidence conditions are associated with the subtropical Pacific high-pressure system [64]. This system migrates throughout the year, with its southernmost position during austral summer and its northernmost position during austral winter (see Figure 1 in [64]). Over mid-latitudes, the DCP is influenced by westerly winds and the high frequency of transients moving from west to east, generating intense precipitation rates on the west side of the Andes at the southern end of the continent and weak precipitation rates on the east side [67]. Finally, the DCP of Southern Chile is influenced by atmospheric rivers, being more frequent during austral winter [68].

4.2. Normalized Amplitude and Phase of Scale-Diurnal Processes

The A_N and ϕ of the first diurnal harmonic (1° H) provide crucial insights into the shape of the diurnal distribution (i.e., unimodal or bimodal [44]) and the timing of peak precipitation rates, respectively. In bimodal distributions (two peaks), the ϕ refers to the stronger of the two peaks. In addition, the ϕ provides valuable information about the timing and spatial distribution of peak precipitation rates associated with each stage of the life cycle of rain-producing systems, as well as their displacement trajectories.

For instance, Squall Lines (SLs) that develop along coastal regions of northern and northeastern SA exhibit a diurnal cycle with a single prominent peak throughout the year [8,11,12,14,21]. These SLs are initiated by sea-breeze circulations producing peak precipitation in their initial stage during the early afternoon (12–14 LST; Figure 6) [8,11,14,50,51]. These SLs subsequently propagate inland, driven by large-scale easterly winds, and reach their mature stage by mid-afternoon to evening, when they produce a more intense precipitation rate peak [8,11,14,50,51]. Eventually, as these systems decay—typically during the early morning hours—they generate a less intense peak before dissipating, often without reaching the Central Amazon. However, through their dissipation, they serve as a source of moisture and may act as a driver for the development of MCSs in other western regions several hours later [69] due to the action of the South American [53,58] and Amazonian [70] Low-Level Jets (LLJs). Both systems (ALLJ and SLLJ) play key roles in sustaining convective activity and moisture transport across SA [53–55,57,58].

The coastal regions of the NWSA—including Colombia, Ecuador, and Northern Peru—as well as the adjacent Pacific Ocean, also exhibit diurnal cycles characterized by a single predominant precipitation rate peak. This finding is consistent with previous studies by [3,11,12,14]. The peaks occur primarily between late afternoon and evening, as a result of the MCSs originating from convection induced by surface heating, leading to sea breezes, and at night due to mountain breezes [3,20,71]. In the adjacent Pacific Ocean, peaks occur in the early morning hours as a result of land breezes produced by the nighttime thermal contrast between the cold continent and the warm tropical Eastern Pacific Ocean [14].

As in [14], we find that the tropical and subtropical regions of the Andes (above 1500 m a.s.l.) display a prominent diurnal cycle with a single peak. The highlands of the Andes exhibit afternoon–night peaks mainly induced by the warming of the Andean slopes,

which leads to deep convection and valley–mountain-type local circulations that trigger the formation of MCSs [1,3,5–7,18,19,32]. Tropical Andean valleys (lower parts of the Andean mountains approximately 1500 masl) exhibit both bimodal and unimodal DCPs, depending on their geographic location. However, precipitation peaks predominantly occur between the midnight and early morning hours. The occurrence of nocturnal peaks may be attributed to the interaction between local mountain–valley-type circulations—i.e., katabatic winds induced by thermal contrasts between the cold valleys and the warmer mountain slopes—and LLJs. The entire Andean region of Peru and Bolivia (below 1500 masl, forming a northwest–southeast-oriented band) is notably influenced by the southern branch of the SALLJ [53,58], which is strongest and most frequent during the early morning hours. This system transports recycled moisture from the Amazon Basin (AB, [30,57]), and serves as fuel for the formation of MCSs that contribute to early morning precipitation peaks. The interaction between the SALLJ and mountain–valley breezes promotes the development of MCSs, resulting in marked precipitation gradients year-round [5,18,29,32–34,53]. In the Andes of Ecuador and Colombia, early morning peaks are similarly modulated by the northern branch of the SALLJ [58] and the Chocó LLJ [19,59], respectively. These LLJs play a comparable role to that observed in the Peruvian and Bolivian Andes. In Venezuela, the Orinoco LLJ, which intensifies during the night and early morning hours [72], also contributes significantly to the modulation of the DCP, establishing nighttime to early morning precipitation rate maxima.

Some regions, such as Southeastern Brazil during the austral summer and the region east of the Andean Mountains in Argentina during the austral spring and summer, exhibit diurnal cycles with a single predominant peak (Figure 4). In Southeastern Brazil, peaks are mainly observed between mid-afternoon and evening [11,14,21], with the primary mechanism being the MCSs formed by the sea breeze propagating inland, coupled with the convergence of humidity and low-level winds. In contrast, in Argentina, peaks occur between night and early morning [14], possibly due to the mountain breeze. Over the large Amazonian rivers (e.g., Rio Negro, Solimões, Amazonas), a diurnal cycle with a single peak is observed near these large bodies of water [4,8,73–75]. The peaks in these terrestrial grid cells occur mainly between the afternoon and night, as a result of the MCSs generated by the thermal gradient, giving rise to river breezes that trigger local convection [4,8,73–75]. The opposite occurs at night, with local convection developing over the grid cells located near the Amazonian rivers as a result of the land breeze [4,8,73–75].

Different studies that used satellite products to investigate the DCP [8,11,14,21] found that the AB is characterized by two predominant times of peak occurrence, identified by values less than 0.5 for the ratio of the A_N to the f_0. The peaks in this region of the AB occur between the afternoon (in the area closer to the Atlantic Ocean) and the night–morning period in the central AB, depending on the displacement of the MCSs. These MCSs are formed by a combination of moisture from dissipating coastal SLs [70], moisture transport from the trade winds of the tropical Atlantic [30,57], and moisture input from the Amazonian Low-Level Jet (ALLJ, [69]). The MCSs formed on the western side of the AB move southward and northeastward (toward the central region of the AB), contributing substantial precipitation, with peaks occurring between evening, night, and morning [2,8,76]. SESA, characterized as a region of MCSs formation throughout the year [53–55], exhibits a weak diurnal cycle, with peaks occurring between early morning and morning, possibly influenced by the characteristics of the SALLJ, which transports moisture to this region [30,53,57,58]. South of the subtropical SA region and in the adjacent Atlantic and Pacific Oceans, the DCP is weaker [11,12,14,21], with a noisy signal in the timing of peak occurrence [11,12,21], likely due to the frequent passage of mid-latitude transient systems.

4.3. Identification of Regions with a Homogeneous DCP

The spatial configuration of clusters across tropical and subtropical SA reflects the combined influence of large-scale and local atmospheric mechanisms. The SAMS modulates the seasonal and regional organization of MCSs ($f_0 < 0.254$ mm/h) [28–30,53,56,58,77,78], while local surface processes—such as sensible and latent heat fluxes land-water contrasts, and topographic gradients—shape the diurnal structure of precipitation [8].

Clusters along the Atlantic and northern/northwestern coasts exhibit robust afternoon peaks year round, influenced by sea breeze-induced squall lines (SL) and MCSs [3,19,20,50,51,71]. In contrast, clusters along the Pacific coast (Peru–Chile) show sparse rainfall, constrained by large-scale subsidence associated with the South Pacific High pressure system and the descending branch of the Hadley cell. Over the Amazon region, most clusters exhibit a bimodal DCP—linked to both nocturnal MCSs triggered by the SALLJ/ALLJ [53,58,70,79], daytime convection and systematic propagation of MCSs from both the eastern and western regions of the AB [2,40,41,69,76]. However, clusters near major rivers tend to exhibit unimodal afternoon peaks, shaped by interactions between the easterly flow and river breeze circulations [4,73–75]. The Eastern Andes clusters, extending from Central Peru to Bolivia—labeled as 1:DJF, 4:MAM, 5:JJA, 5:SON—maintain a consistent unimodal pattern with early morning precipitation peaks. These are driven by the interplay between SALLJ events and orographic circulations [5,32,33], and cold air intrussions from mid-latitudes [18]. In SESA, clusters do not exhibit a well-defined diurnal peak and are primarily influenced by year-round MCSs activity—generated by the transport of humidity from the Amazon [30,57]—and mid-latitude disturbances. At higher latitudes, the spatial organization of clusters is more disorganized, likely as a response to the high frequency of transient systems.

Applying clustering algorithms that incorporate spatial variables such as latitude, longitude, and altitude could help distinguish regions along the eastern coast of SA from those over the Andes (e.g., Cluster 1 in Figure 7A). The Spatial Kluster Analysis by Tree Edge Removal (SKATER; [80]) algorithm emerges as a promising tool for identifying homogeneous regions. An example of its application can be found in [81]. However, this algorithm is computationally expensive due to the dissimilarity technique employed in cluster formation.

4.4. Historical Trends in the DCP

Statistically significant trends in the DCP are detected only in the tropical region of SA, particularly over the Amazon. During DJF, increases in f_0 and C_1 (Figures 8A and 9A) are observed in NESA, especially near major Amazonian rivers (Solimões, Negro, Amazonas), as well as along the eastern slopes of the Central Andes and Southern Peru. Conversely, a northwest–southeast-oriented negative trend is identified in the central Amazon, likely linked to land cover changes such as deforestation and agricultural expansion [82]. Similar spatial patterns are reported by ([83], and references therein), although on different temporal scales, particularly regarding positive trends in NESA and NWSA, and negative trends in the Central and Southern Amazon. In MAM (Figures 8B and 9B), DCP intensity is decreased in NESA and along the Amazon River, while localized increases are observed in parts of the Brazilian state of Amazonas (Manaus). During JJA (Figures 8C and 9C), positive trends are evident in Southern Venezuela and the Eastern Colombian Andes, with a negative core in Southeastern Venezuela. No significant trends are detected in SON.

The negative trend observed in A_N over the Amazon and along the Amazon River (Figure 10), may reflect a shift in the diurnal precipitation structure, potentially characterized by a bimodal pattern. One peak appears linked to nocturnal MCSs, influenced by the

South American Low-Level Jet (SALLJ) and land–river breeze dynamics. A second peak likely results from afternoon convection enhanced by increased surface heating.

These observed DCP trends are consistent with a gradual decline in the MCSs occurrence over the past two decades [40], possibly driven by global warming. El Niño–Southern Oscillation (ENSO), although lower in frequency, can modulate the DCP by altering large-scale circulation patterns and MCSs activity ([83], and references therein). Additionally, local- and regional-scale processes such as deforestation [84–86], land cover change [82], and increased biomass-burning aerosols [87] likely contribute to observed DCP changes in the Amazon.

Although trend studies focusing specifically on the DCP are lacking for SA, the use of extreme precipitation indices—as in [83]—suggests that changes in sub-daily precipitation variability may be manifesting at broader temporal scales. Our results demonstrate that trends in f_0, C_1, and A_N are spatially heterogeneous, likely influenced by interactions among surface processes, large-scale moisture transport, alterations in large-scale subsidence and convergence processes, and intensified surface warming. These findings underscore the importance of considering diurnal variability when assessing precipitation trends in the tropics.

5. Summary and Conclusions

This study investigated the variability and trends of the diurnal cycle of precipitation (DCP) across South America (SA), using a 20-year climatology (2001–2020) of diurnal metrics derived from the IMERG product. The hourly mean precipitation rate (f_0) showed that Mesoscale Convective Systems (MCSs, $f_0 > 0.254$ mm/h; [41]) are the main systems that organize precipitation across tropical and subtropical SA [42], and therefore play a key role in modulating the DCP. The spatial–temporal distribution of MCSs, and consequently the variability of the DCP, is strongly influenced by large-scale mechanisms such as the South American Monsoon System (SAMS, [28–31,78]) and by processes responsible for the initiation of convection [56,63]. Nevertheless, local factors, including their spatial configuration—such as water bodies, topography, and other surface heterogeneities—modulate the intensity of the hourly mean precipitation rates and the characteristics of MCSs [40,41,50,51,60,61,73]. Regions including extreme Southern Chile, southeastern SA (SESA), the coastal region in northwestern SA (NWSA), and the Eastern Central Andes of Peru and Bolivia exhibit high f_0 values throughout the year. The southern tip of Chile is influenced by the nearly continuous passage of synoptic-scale disturbances from west to east. SESA is characterized as a region of frequent MCSs formation and substantial year-round precipitation [15], with the South American Low-Level Jet (SALLJ) playing a critical role in moisture transport [53,56,58,79]. In the NWSA and the Eastern Central Andes (Peru and Bolivia), thermally driven local circulations—resulting from ocean-continent and valley–mountain interactions—significantly contribute to MCSs formation throughout the year [3,5,19,32,33,59].

As with the f_0, the spatial and temporal variability of A_N and ϕ of the first harmonic (1° H) showed a clear seasonal pattern, linked with the variability of the SAMS and with the processes responsible for the initiation of convection. Additionally, these diurnal metrics highlight fine-scale DCP characteristics that are primarily influenced by local factors. The results showed that along the coastal regions—and a few hundred kilometers inland—in NESA and NWSA, as well as the coastal regions of southern and Southeastern Brazil and in the high-elevation areas of the Andes, unimodal DCPs were observed, characterized by a single precipitation peak. The interior of the continent over the tropical region of SA generally showed a bimodal DCP, particularly from December to May, with precipitation peaks occurring between the late evening and early morning hours. However, in and around

major Amazonian rivers (e.g., Negro River and the Amazon River), a consistent unimodal DCP was observed throughout the year, largely driven by river breeze circulations that triggered convective cells mainly in the afternoon. The ϕ metric provides information about the timing of precipitation rate peaks and the direction of propagation of rain-producing systems. Squall lines (SLs) forming along the coastal region of NESA typically peak during the afternoon hours—likely during their initial development—and subsequently move inland, with peak precipitation shifting to the late afternoon and evening periods [50,51]. As noted by [69], these MCSs, initially formed along the coast, often dissipate before reaching central Amazonia. However, their dissipation contributes to local moisture availability, which supports the development of new MCSs. Surface heating induced by solar radiation plays a crucial role in triggering these new MCSs, which continue to propagate westward. A similar pattern is observed in the Western Amazon Basin, where precipitation systems move southward and eastward. In the mid-latitudes, the ϕ signal appears noisier, likely due to the frequent passage of synoptic disturbances, which can generate peaks in f_0 at various times throughout the day.

The application of cluster analysis enabled the identification of eight distinct types of DCP during the DJF, MAM, and JJA periods (and nine during SON), based on diurnal metrics. While the spatial configuration of clusters throughout the year reveals a clear seasonal pattern, the grouping of grid cells within specific clusters also reflects the influence of local factors on the diurnal distribution, the intensity of the f_0, and the timing of maximum precipitation rates. Statistically significant trends in the DCP over the past two decades were identified exclusively in the Amazon Basin (AB). These positive and/or negative trends may be associated with observed changes in the occurrence of MCSs over the AB [41]. These changes are likely associated with variations in large-scale moisture transport and in the positioning of subsidence and convergence zones, potentially modulated by climate patterns such as the El Niño–Southern Oscillation (ENSO) and the Madden–Julian Oscillation (MJO). In addition, land use change and deforestation could influence these trends by reducing moisture availability, thereby inhibiting the formation of precipitation systems [82,84–86]. To our knowledge, no prior studies have assessed DCP trends across South America or the Amazon at a sub-daily resolution. However, previous analyses of precipitation trends on daily to annual scales in the region (e.g., [82,83]) suggest the need to investigate whether such trends are also evident at finer temporal scales. Since extreme precipitation events often occur on sub-daily timescales, long-term changes in these events are expected to be captured by DCP metrics.

This study highlights how large-scale mechanisms and local-scale processes, interacting with the surrounding environment, influence the DCP in South America, generating heterogeneous behaviors and even showing trends of change over the past two decades. To shed light on and clarify the mechanisms underlying the variability of the DCP, high-resolution numerical modeling studies are necessary to understand the role of each driver and their multiscale interactions that trigger different precipitation systems. Furthermore, the growing application of machine learning and artificial intelligence algorithms offers promising opportunities to assess the degree of contribution of different drivers to the initiation of diurnal-scale precipitation events.

Supplementary Materials: The following supporting information can be downloaded at: https://www.mdpi.com/article/10.3390/meteorology4020013/s1.

Author Contributions: Conceptualization, R.G.R.-N., M.A.F.d.S.D. and P.L.d.S.D.; methodology, R.G.R.-N.; software, R.G.R.-N.; validation, R.G.R.-N.; formal analysis, R.G.R.-N., M.A.F.d.S.D. and P.L.d.S.D.; investigation, R.G.R.-N., M.A.F.d.S.D. and P.L.d.S.D.; resources, R.G.R.-N., M.A.F.d.S.D. and P.L.d.S.D.; data curation, R.G.R.-N.; writing—original draft preparation, R.G.R.-N.; writing—review and editing, R.G.R.-N., M.A.F.d.S.D. and P.L.d.S.D.; visualization, R.G.R.-N.; supervision, M.A.F.d.S.D. and P.L.d.S.D.; project administration, M.A.F.d.S.D. and P.L.d.S.D.; funding acquisition, M.A.F.d.S.D. and P.L.d.S.D. All authors have read and agreed to the published version of the manuscript.

Funding: This research was funded by *Conselho Nacional de Desenvolvimento Científico e Tecnológico (CNPq)* grant number 140883/2023-1.

Institutional Review Board Statement: Not applicable.

Informed Consent Statement: Not applicable.

Data Availability Statement: The dataset used in this study is available at https://disc.gsfc.nasa.gov/datasets, (accessed on 1 November 2021).

Acknowledgments: The GPM IMERG Final Precipitation L3 Half Hourly 0.1° × 0.1°V06 product is provided by the Global Precipitation Measurement (GPM) project and is available in the online repository of the National Aeronautics and Space Administration (NASA).

Conflicts of Interest: The authors declare no conflicts of interest.

Abbreviations

The following abbreviations are used in this manuscript:

A_N	Normalized Amplitude
A_{N2}	Normalized Amplitude of the second harmonic
AB	Amazon Basin
ALLJ	Amazonian Low-Level Jet
CMIP5	Coupled Model Intercomparison Project Phase 5
CMIP6	Coupled Model Intercomparison Project Phase 6
DCP	Diurnal Cycle of Precipitation
DJF	December–January–February
ECMWF	European Centre for Medium-Range Weather Forecasts
EOF	Empirical Orthogonal Function
ENSO	El Niño-Southern Oscillation
ERA5	ECMWF Reanalysis v5
f_0	Mean precipitation rate
GCM	General Circulation Model
GPM	Global Precipitation Measurement
IMERG	Integrated Multi-satellite Retrievals for the GPM
ITZC	Inter-Tropical Convergence Zone
JJA	June–July–August
LLJ	Low-Level Jets
LST	Local Solar Time
masl	meters above sea level
MAM	March–April–May
MCS	Mesoscale Convective System
MCSs	Mesoscale Convective Systems
MJO	Madden-Julian Oscillation
NESA	Northeastern South America
NWSA	Northwestern South America
PC	Principal Component
SA	South America

SACZ	South Atlantic Convergence Zone
SALLJ	South American Low-Level Jet
SAMS	South American Monsoon System
SESA	Southeastern South America
SLs	Squall Lines
SON	September–October–November
SSE	Sum of the Square Error
UTC	Coordinated Universal Time
ϕ	Phase
$1\,^{\circ}H$	First Harmonic
$2\,^{\circ}H$	Second Harmonic

Appendix A

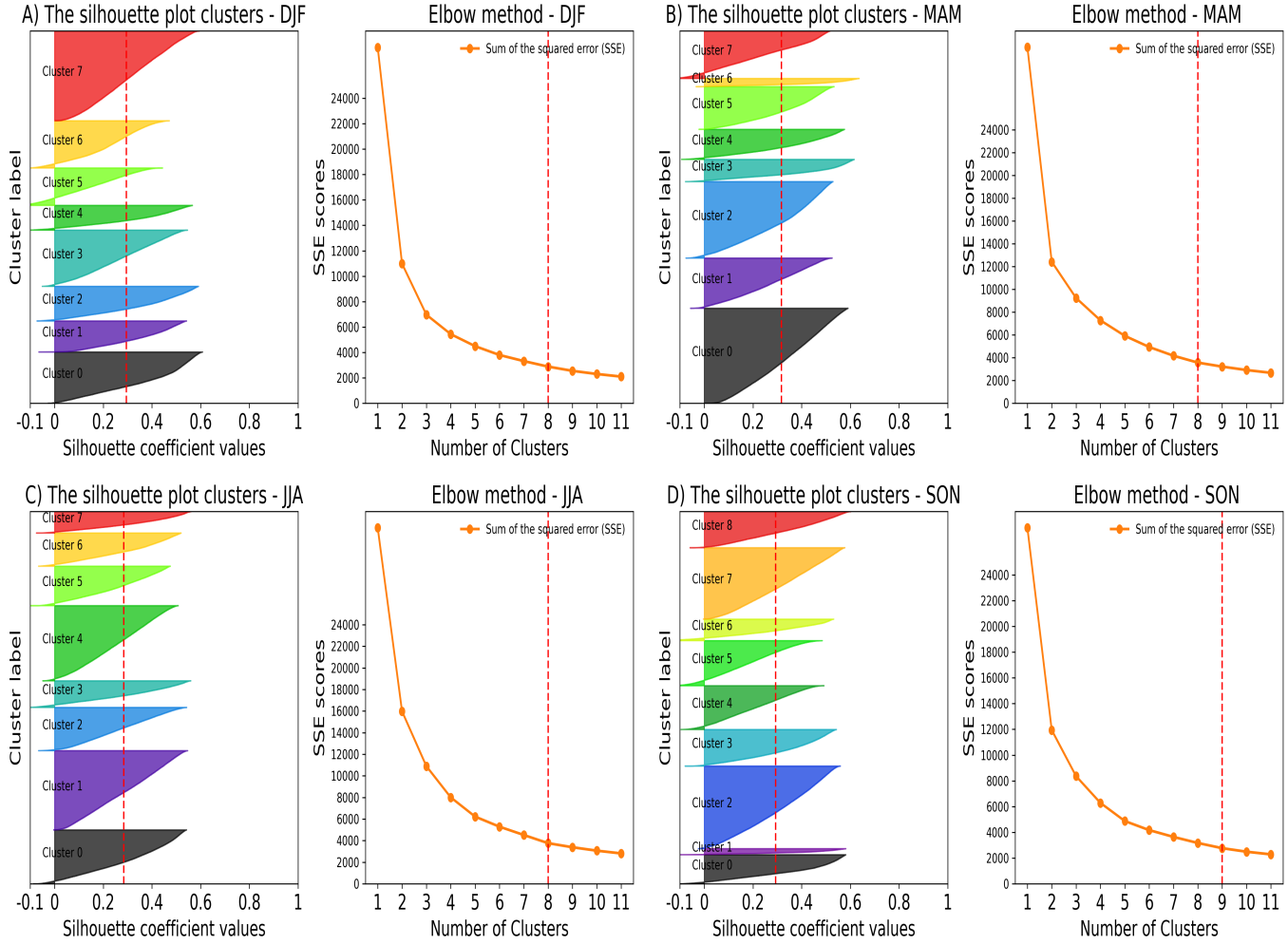


Figure A1. Silhouette scores (**left**) and elbow method (**right**). In all the graphics, the red line in the silhouette scores indicate the mean value as a function of the number of clusters, and in the elbow method, it represents the SSE value for a specific number of clusters. (**A**) December–January–February (DJF). (**B**) March–April–May (MAM). (**C**) June–July–August (JJA). (**D**) September–October–November (SON).

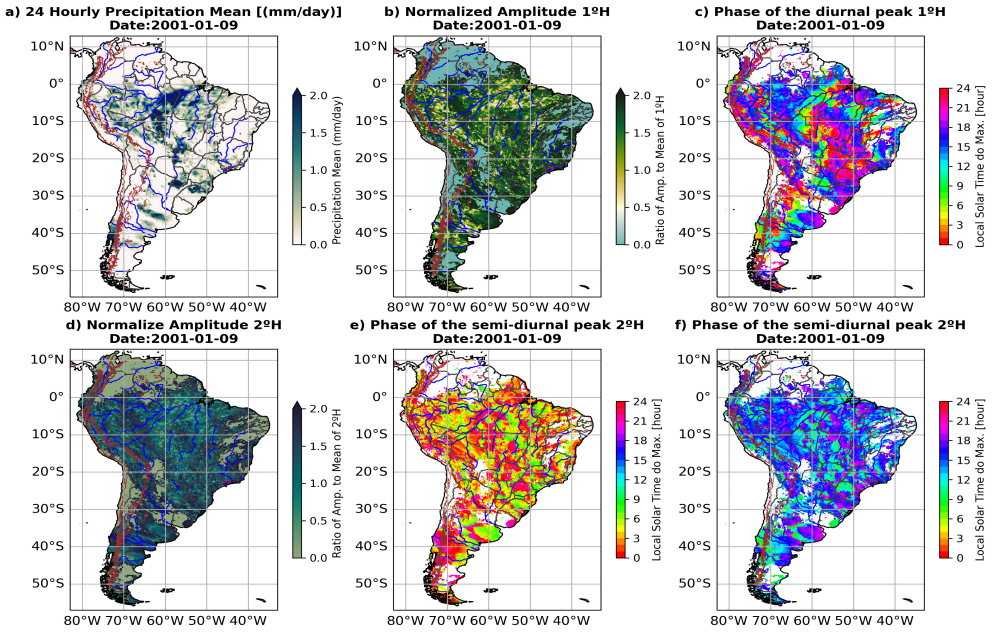


Figure A2. Diurnal metrics from 2001-01-09. (**a**) 24 hourly precipitation mean. (**b**) Normalized amplitude 1° H. (**c**) Phase of the diurnal peak of 1° H (LST). (**d**) Normalized amplitude 2° H. (**e**) Phase of the first diurnal peak of 2° H (LST). (**f**) Phase of the second diurnal peak 2° H (LST).

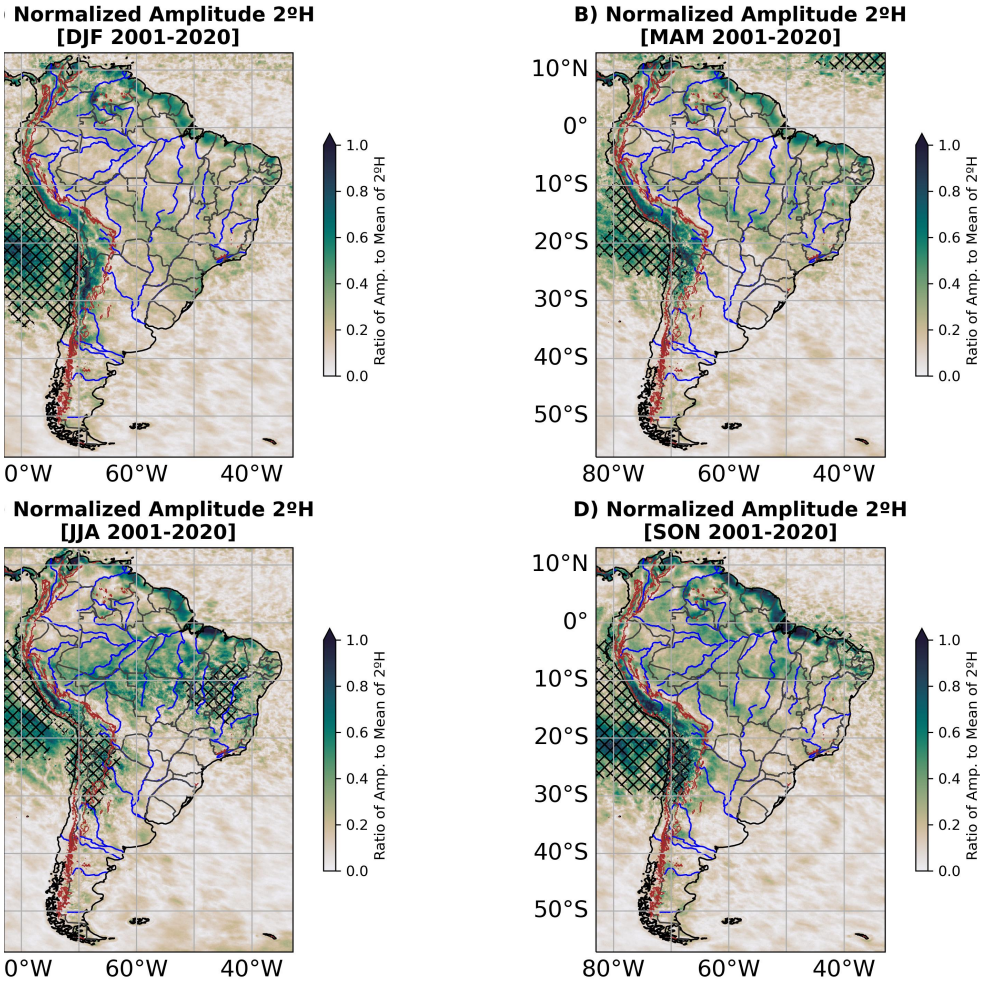


Figure A3. Normalized amplitude of the 2 °H (A_{N2}). (**A**) December–January–February (DJF). (**B**) March–April–May (MAM). (**C**) June–July–August (JJA). (**D**) September–October–November (SON). The blue lines depict the main rivers of South America (SA). The brown lines extending from the extreme south to the extreme north of SA mark the 1500 m a.s.l. elevation of the Andes and other highlands regions. Pixels with intensities below 0.01 mm/h are marked with crosses ("xx") and represent regions with scarce precipitation.

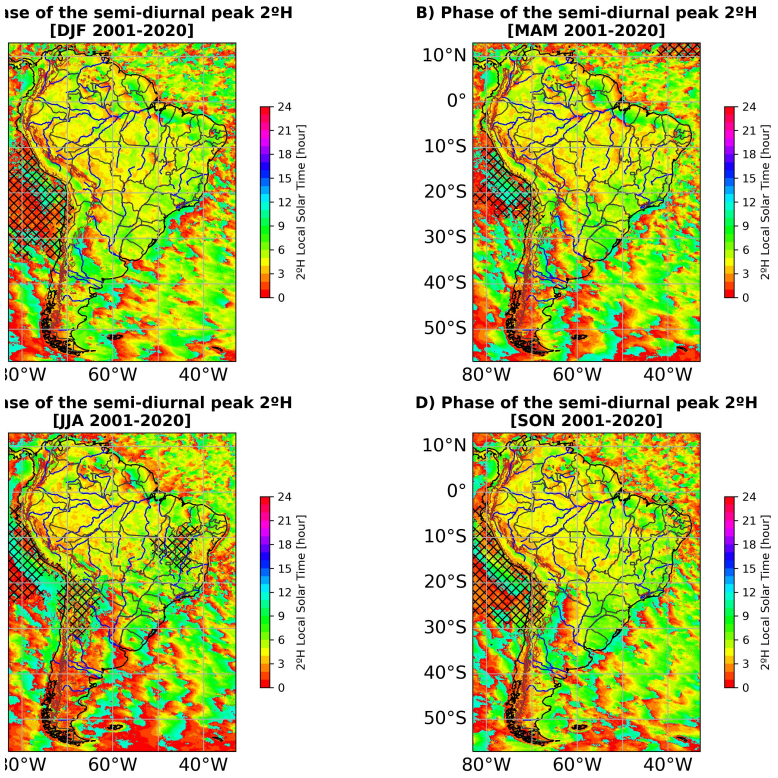


Figure A4. Timing of occurrence of the first maxima (Local Solar Time, LST) of the semi-diurnal processes through the phase (ϕ) of the 2° H. (**A**) December–January–February (DJF). (**B**) March–April–May (MAM). (**C**) June–July–August (JJA). (**D**) September–October–November (SON). The blue lines depict the main rivers of South America (SA). The brown lines extending from the extreme south to the extreme north of SA mark the 1500 m a.s.l. elevation of the Andes and other highlands regions. Pixels with intensities below 0.01 mm/h are marked with crosses ("xx") and represent regions with scarce precipitation.

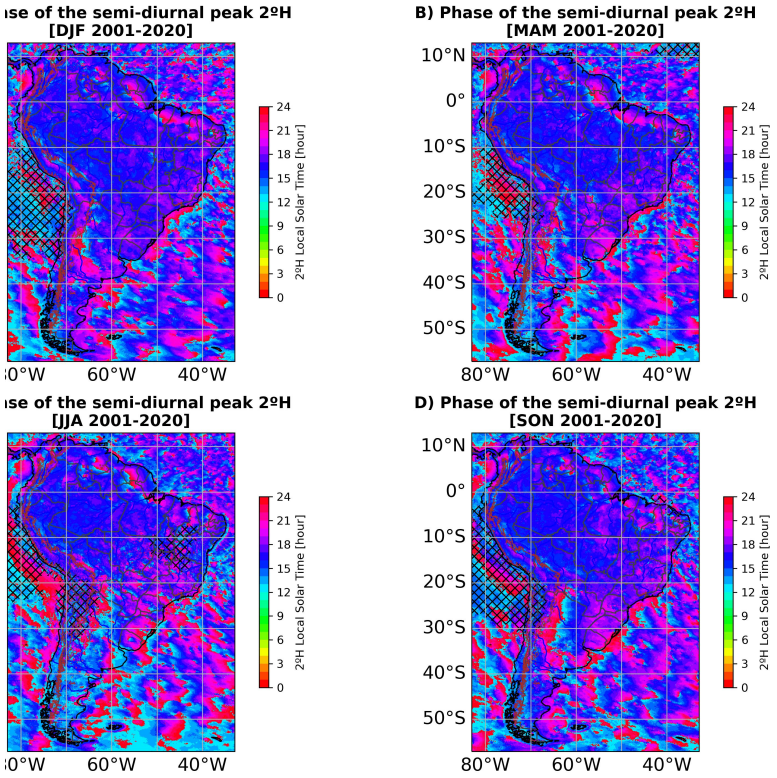


Figure A5. Timing of occurrence of the second maxima (Local Solar Time, LST) of the semi-diurnal processes through the phase (ϕ) of the 2° H. (**A**) December–January–February (DJF). (**B**) March–April–May (MAM). (**C**) June–July–August (JJA). (**D**) September–October–November (SON). The blue lines depict the main rivers of South America (SA). The brown lines extending from the extreme south to the extreme north of SA mark the 1500 m a.s.l. elevation of the Andes and other highlands regions. Pixels with intensities below 0.01 mm/h are marked with crosses ("xx") and represent regions with scarce precipitation.

References

1. Yang, G.Y.; Slingo, J. The diurnal cycle in the tropics. *Mon. Weather. Rev.* **2001**, *129*, 784. [CrossRef]
2. Angelis, C.F.; McGregor, G.R.; Kidd, C. Diurnal cycle of rainfall over the Brazilian Amazon. *Clim. Res.* **2004**, *26*, 139. [CrossRef]
3. Poveda, G.; Mesa, O.J.; Salazar, L.F.; Arias, P.A.; Moreno, H.A.; Vieira, S.C.; Agudelo, P.A.; Toro, V.G.; Alvarez, J.F. The diurnal cycle of precipitation in the tropical Andes of Colombia. *Mon. Weather. Rev.* **2005**, *133*, 228. [CrossRef]
4. Tanaka, L.M.D.S.; Satyamurty, P.; Machado, L.A.T. Diurnal variation of precipitation in Central Amazon Basin. *Int. J. Climatol.* **2014**, *34*, 3574. [CrossRef]
5. Junquas, C.; Takahashi, K.; Condom, T.; Espinoza, J.C.; Chávez, S.; Sicart, J.E.; Lebel, T. Understanding the influence of orography on the precipitation diurnal cycle and the associated atmospheric processes in the central Andes. *Clim. Dyn.* **2018**, *50*, 3995–4017. [CrossRef]
6. Espinoza, J.C.; Garreaud, R.; Poveda, G.; Arias, P.A.; Molina-Carpio, J.; Masiokas, M.; Viale, M.; Scaff, L. Hydroclimate of the Andes Part I: Main Climatic Features. *Front. Earth Sci.* **2020**, *8*, 65. [CrossRef]
7. Ruiz-Hernández, J.C.; Condom, T.; Ribstein, P.; Le Moine, N.; Espinoza, J.C.; Junquas, C.; Villacís, M.; Vera, A.; Muñoz, T.; Maisincho, L.; et al. Spatial variability of diurnal to seasonal cycles of precipitation from a high-altitude equatorial Andean valley to the Amazon Basin. *J. Hydrol. Reg. Stud.* **2021**, *38*, 100924. [CrossRef]
8. Ramírez-Nina, R.G.; Silva Dias, M.A.F. Heterogeneity of the diurnal cycle of precipitation in the Amazon Basin. *Front. Clim.* **2024**, *6*, 1370097. [CrossRef]
9. Betts, A.K.; Jakob, C. Study of diurnal cycle of convective precipitation over Amazonia using a single column model. *J. Geophys. Res. Atmos.* **2002**, *107*, 4732. [CrossRef]
10. Dirmeyer, P.A.; Cash, B.A.; Kinter, J.L.; Shukla, J.; Pan, H.L.; Straus, D.M. Simulating the diurnal cycle of rainfall in global climate models: Resolution versus parameterization. *Clim. Dyn.* **2012**, *39*, 399–418. [CrossRef]

11. Covey, C.; Gleckler, P.J.; Doutriaux, C.; Williams, D.N.; Dai, A.; Fasullo, J.; Trenberth, K.; Berg, A. Metrics for the diurnal cycle of precipitation: Toward routine benchmarks for climate models. *J. Clim.* **2016**, *29*, 4461–4471. [CrossRef]
12. Watters, D.; Battaglia, A.; Allan, R.P. The diurnal cycle of precipitation according to multiple decades of global satellite observations, three CMIP6 models, and the ECMWF reanalysis. *J. Clim.* **2021**, *34*, 5063–5080. [CrossRef]
13. Paccini, L.; Stevens, B. Assessing precipitation over the Amazon basin as simulated by a storm-resolving model. *J. Geophys. Res. Atmos.* **2023**, *128*, e2022JD037436. [CrossRef]
14. Giles, J.A.; Ruscica, R.C.; Menéndez, C.G. The diurnal cycle of precipitation over South America represented by five gridded datasets. *Int. J. Climatol.* **2020**, *40*, 668–686. [CrossRef]
15. da Rocha, R.P.; Llopart, M.; Reboita, M.S.; Silva, L.C.; Silva, A.P.; Carrasco, G.G. Precipitation Diurnal Cycle Assessment in Convection-Permitting Simulations in Southeastern South America. *Earth Syst. Environ.* **2024**, *8*, 1–19. [CrossRef]
16. Hersbach, H.; Bell, B.; Berrisford, P.; Hirahara, S.; Horányi, A.; Muñoz-Sabater, J.; Nicolas, J.; Peubey, C.; Radu, R.; Schepers, D.; et al. The ERA5 global reanalysis. *Q. J. R. Meteorol. Soc.* **2020**, *146*, 1999–2049. [CrossRef]
17. Saraiva, I.; Dias, M.A.F.S.; Morales, C.A.R.; Saraiva, J.M.B. Regional Variability of Rain Clouds in the Amazon Basin as Seen by a Network of Weather Radars. *J. Appl. Meteorol. Climatol.* **2016**, *55*, 2657–2676. [CrossRef]
18. Chavez, S.P.; Silva, Y.; Barros, A.P. High-elevation Monsoon Precipitation Processes in the Central Andes of Peru. *J. Geophys. Res. Atmos.* **2020**, *125*, e2020JD032947. [CrossRef]
19. Bedoya-Soto, J.M.; Aristizábal, E.; Carmona, A.M.; Poveda, G. Seasonal Shift of the Diurnal Cycle of Rainfall Over Medellin's Valley, Central Andes of Colombia (1998–2005). *Front. Earth Sci.* **2019**, *7*, 92. [CrossRef]
20. Bendix, J.; Rollenbeck, R.; Reudenbach, C. Diurnal Patterns of Rainfall in a Tropical Andean Valley of Southern Ecuador as Seen by a Vertically Pointing K-band Doppler Radar. *Int. J. Climatol.* **2006**, *26*, 829–846. [CrossRef]
21. Watters, D.; Battaglia, A. The summertime diurnal cycle of precipitation derived from IMERG. *Remote Sens.* **2019**, *11*, 1781. [CrossRef]
22. Tan, J.; Petersen, W.A.; Tokay, A. A Novel Approach to Identify Sources of Errors in IMERG for GPM Ground Validation. *J. Hydrometeorol.* **2016**, *17*, 2477–2491. [CrossRef]
23. Gadelha, A.N.; Coelho, V.H.R.; Xavier, A.C.; Barbosa, L.R.; Melo, D.C.D.; Xuan, Y.; Huffman, G.J.; Petersen, W.A.; Almeida, C.d.N. Grid box-level evaluation of IMERG over Brazil at various space and time scales. *Atmos. Res.* **2019**, *218*, 231–244. [CrossRef]
24. Tapiador, F.J.; Navarro, A.; García-Ortega, E.; Merino, A.; Sánchez, J.L.; Marcos, C.; Kummerow, C. The Contribution of Rain Gauges in the Calibration of the IMERG Product: Results from the First Validation over Spain. *J. Hydrometeorol.* **2020**, *21*, 161–182. [CrossRef]
25. Pradhan, R.K.; Markonis, Y.; Godoy, M.R.V.; Villalba-Pradas, A.; Andreadis, K.M.; Nikolopoulos, E.I.; Papalexiou, S.M.; Rahim, A.; Tapiador, F.J.; Hanel, M. Review of GPM IMERG performance: A global perspective. *Remote Sens. Environ.* **2022**, *268*, 112754. [CrossRef]
26. Dai, A.; Lin, X.; Hsu, K.L. The Frequency, Intensity, and Diurnal Cycle of Precipitation in Surface and Satellite Observations over Low- and Mid-Latitudes. *Clim. Dyn.* **2007**, *29*, 727–744. [CrossRef]
27. Zhou, J.; Lau, K.M. Does a Monsoon Climate Exist over South America? *J. Clim.* **1998**, *11*, 1020–1040. [CrossRef]
28. Carvalho, L.M.; Jones, C.; Silva, A.E.; Liebmann, B.; Silva, D.P. The South American Monsoon System and the 1970s Climate Transition. *Int. J. Climatol.* **2011**, *31*, 1248. [CrossRef]
29. Vera, C.; Higgins, W.; Amador, J.; Ambrizzi, T.; Garreaud, R.; Gochis, D.; Gutzler, D.; Lettenmaier, D.; Marengo, J.; Mechoso, C.R.; et al. Toward a unified view of the American monsoon systems. *J. Clim.* **2006**, *19*, 4977–5000. [CrossRef]
30. Marengo, J.A.; Liebmann, B.; Grimm, A.M.; Misra, V.; Silva Dias, P.L.; Cavalcanti, I.F.A.; Carvalho, L.M.V.; Berbery, E.H.; Ambrizzi, T.; Vera, C.S.; et al. Recent developments on the South American monsoon system. *Int. J. Climatol.* **2012**, *32*, 1–21. [CrossRef]
31. Grimm, A.M.; Dominguez, F.; Cavalcanti, I.F.; Cavazos, T.; Gan, M.A.; Silva Dias, P.L.; Fu, R.; Castro, C.; Hu, H.; Barreiro, M. South and North American Monsoons: Characteristics, life cycle, variability, modeling, and prediction. In *The Multiscale Global Monsoon System*; World Scientific: Singapore, 2020; pp. 49–66.
32. Chavez, S.P.; Takahashi, K. Orographic rainfall hot spots in the Andes-Amazon transition according to the TRMM precipitation radar and in situ data. *J. Geophys. Res. Atmos.* **2017**, *122*, 5870–5882. [CrossRef]
33. Espinoza, J.C.; Chavez, S.; Ronchail, J.; Junquas, C.; Takahashi, K.; Lavado, W. Rainfall hotspots over the southern tropical Andes: Spatial distribution, rainfall intensity, and relations with large-scale atmospheric circulation. *Water Resour. Res.* **2015**, *51*, 3459–3475. [CrossRef]
34. Espinoza, J.C.; Ronchail, J.; Guyot, J.L.; Cochonneau, G.; Naziano, F.; Lavado, W.; De Oliveira, E.; Pombosa, R.; Vauchel, P. Spatio-temporal rainfall variability in the Amazon basin countries (Brazil, Peru, Bolivia, Colombia, and Ecuador). *Int. J. Climatol.* **2009**, *29*, 1574. [CrossRef]
35. Albrecht, R.I.; Goodman, S.J.; Buechler, D.E.; Blakeslee, R.J.; Christian, H.J. Where Are the Lightning Hotspots on Earth? *Bull. Am. Meteorol. Soc.* **2016**, *97*, 2051–2068. [CrossRef]

36. Huffman, G.J.; Stocker, E.F.; Bolvin, D.T.; Nelkin, E.J.; Tan, J. GPM IMERG Final Precipitation L3 Half Hourly 0.1 Degree x 0.1 Degree V06, 2019. Available online: https://disc.gsfc.nasa.gov/datasets/GPM_3IMERGHH_07/summary (accessed on 1 November 2021).
37. Huffman, G.; Braithwaite, D.; Hsu, K.; Joyce, R.; Kidd, C.; Nelkin, E.; Sorooshian, S.; Stocker, E.F.; Tan, J.; Wolff, D.B. Integrated Multi-satellite Retrievals for the Global Precipitation Measurement (GPM) Mission (IMERG). In *Satellite Precipitation Measurement*; Levizzani, V., Kidd, C., Kirschbaum, D.B., Kummerow, C.D., Nakamura, K., Turk, F.J., Eds.; Advances in Global Change Research; Springer: Cham, Switzerland, 2020; Volume 67. [CrossRef]
38. Tan, J.; Huffman, G.J.; Bolvin, D.T.; Nelkin, E.J. Diurnal cycle of IMERG V06 precipitation. *Geophys. Res. Lett.* **2019**, *46*, 13584–13592. [CrossRef]
39. Dominguez, F.; Rasmussen, R.; Liu, C.; Ikeda, K.; Prein, A.; Varble, A.; Arias, P.A.; Bacmeister, J.; Bettolli, M.L.; Callaghan, P.; et al. Advancing South American Water and Climate Science through Multidecadal Convection-Permitting Modeling. *Bull. Am. Meteorol. Soc.* **2024**, *105*, E32–E44. [CrossRef]
40. Rehbein, A.; Ambrizzi, T. Mesoscale convective systems over the Amazon basin in a changing climate under global warming. *Clim. Dyn.* **2023**, *61*, 1815–1827. [CrossRef]
41. Rehbein, A.; Ambrizzi, T.; Mechoso, C.R.; Espinosa, S.A.; Myers, T.A. Mesoscale convective systems over the Amazon basin: The GoAmazon2014/5 program. *Int. J. Climatol.* **2019**, *39*, 5599–5618. [CrossRef]
42. Nesbitt, S.W.; Cifelli, R.; Rutledge, S.A. Storm morphology and rainfall characteristics of TRMM precipitation features. *Mon. Weather. Rev.* **2006**, *134*, 2702. [CrossRef]
43. Wilks, D.S. *Statistical Methods in the Atmospheric Sciences*, 3rd ed.; International Geophysics Series; Academic Press: Oxford, UK, 2011; Volume 100.
44. Easterling, D.R.; Robinson, P.J. The diurnal variation of thunderstorm activity in the United States. *J. Appl. Meteorol. Climatol.* **1985**, *24*, 1048–1058. [CrossRef]
45. Lorenz, E.N. *Empirical Orthogonal Functions and Statistical Weather Prediction*; Massachusetts Institute of Technology, Department of Meteorology: Cambridge, UK, 1956; Volume 1.
46. Van Der Maaten, L.; Postma, E.O.; Van Den Herik, H.J. Dimensionality reduction: A comparative review. *J. Mach. Learn. Res.* **2009**, *10*, 13.
47. Mann, H.B. Nonparametric Tests Against Trend. *Econometrica* **1945**, *13*, 245–259. [CrossRef]
48. Kendall, K. Thin-Film Peeling—The Elastic Term. *J. Phys. D Appl. Phys.* **1975**, *8*, 1449–1452. [CrossRef]
49. Sen, P.K. Estimates of the Regression Coefficient Based on Kendall's Tau. *J. Am. Stat. Assoc.* **1968**, *63*, 1379–1389. [CrossRef]
50. Cohen, J.C.; Silva Dias, M.A.; Nobre, C.A. Environmental conditions associated with Amazonian squall lines: A case study. *Mon. Weather. Rev.* **1995**, *123*, 3163. [CrossRef]
51. Alcântara, C.R.; Dias, M.A.S.; Souza, E.P.; Cohen, J.C. Verification of the role of the low level jets in Amazon squall lines. *Atmos. Res.* **2011**, *100*, 36. [CrossRef]
52. Horel, J.D.; Hahmann, A.N.; Geisler, J.E. An investigation of the annual cycle of convective activity over the tropical Americas. *J. Clim.* **1989**, *2*, 1388–1403. [CrossRef]
53. Marengo, J.A.; Soares, W.R.; Saulo, C.; Nicolini, M. Climatology of the low-level jet east of the Andes as derived from the NCEP–NCAR reanalyses: Characteristics and temporal variability. *J. Clim.* **2004**, *17*, 2261. [CrossRef]
54. Liebmann, B.; Kiladis, G.N.; Vera, C.S.; Saulo, A.C.; Carvalho, L.M.V. Subseasonal Variations of Rainfall in South America in the Vicinity of the Low-Level Jet East of the Andes and Comparison to Those in the South Atlantic Convergence Zone. *J. Clim.* **2004**, *17*, 3829–3842. [CrossRef]
55. Salio, P.; Nicolini, M.; Zipser, E.J. Mesoscale Convective Systems over Southeastern South America and Their Relationship with the South American Low-Level Jet. *Mon. Weather. Rev.* **2007**, *135*, 1290–1309. [CrossRef]
56. Arraut, J.M.; Nobre, C.; Barbosa, H.M.; Obregon, G.; Marengo, J. Aerial rivers and lakes: Looking at large-scale moisture transport and its relation to Amazonia and to subtropical rainfall in South America. *J. Clim.* **2012**, *25*, 543. [CrossRef]
57. Drumond, A.; Marengo, J.; Ambrizzi, T.; Nieto, R.; Moreira, L.; Gimeno, L. The role of the Amazon Basin moisture in the atmospheric branch of the hydrological cycle: A Lagrangian analysis. *Hydrol. Earth Syst. Sci.* **2014**, *18*, 2577–2598. [CrossRef]
58. Jones, C.; Mu, Y.; Carvalho, L.M.V.; Ding, Q. The South America Low-Level Jet: Form, variability and large-scale forcings. *NPJ Clim. Atmos. Sci.* **2023**, *6*, 175. [CrossRef]
59. Poveda, G. La hidroclimatología de Colombia: Una síntesis desde la escala inter-decadal hasta la escala diurna. *Rev. Acad. Colomb. Cienc. Exactas Físicas Nat.* **2004**, *28*, 201–222. [CrossRef]
60. Rehbein, A.; Ambrizzi, T.; Mechoso, C.R. Mesoscale convective systems over the Amazon basin. Part I: Climatological aspects. *Int. J. Climatol.* **2017**, *38*, 215–229. [CrossRef]
61. Rehbein, A. Sistemas Convectivos de Mesoescala na Bacia Amazônica: Clima Presente e ProjeçõEs Futuras em Cenários de MudançAs ClimáTicas. Ph.D. Thesis, Instituto de Astronomia, Geofísica e Ciências Atmosféricas, Universidade de São Paulo, São Paulo, Brazil, 2021. [CrossRef]

62. Teodoro, T.A.; Reboita, M.S.; Llopart, M.; da Rocha, R.P.; Ashfaq, M. Climate change impacts on the South American Monsoon System and its surface–atmosphere processes through RegCM4 CORDEX-CORE projections. *Earth Syst. Environ.* **2021**, *5*, 825–847. [CrossRef]
63. Satyamurty, P.; Nobre, C.A.; Silva, D.P. *Meteorology of the Southern Hemisphere*; Springer: Berlin/Heidelberg, Germany; American Meteorological Society: Boston, MA, USA, 1998; pp. 119–139.
64. Cai, W.; McPhaden, M.J.; Grimm, A.M.; Rodrigues, R.R.; Taschetto, A.S.; Garreaud, R.D.; Dewitte, B.; Poveda, G.; Ham, Y.G.; Santoso, A.; et al. Climate impacts of the El Niño–Southern Oscillation on South America. *Nat. Rev. Earth Environ.* **2020**, *1*, 215–231. [CrossRef]
65. Reboita, M.S.; Gan, M.A.; Porfírio, R.; Rocha, D.A.; Ambrizzi, T. Regimes de precipitação na América do Sul: Uma revisão bibliográfica. *Rev. Bras. Meteorol.* **2010**, *25*, 185–204. [CrossRef]
66. Poveda, G.; Waylen, P.R.; Pulwarty, R.S. Annual and inter-annual variability of the present climate in northern South America and southern Mesoamerica. *Palaeogeogr. Palaeoclimatol. Palaeoecol.* **2006**, *234*, 3–27. [CrossRef]
67. Gimeno, L.; Dominguez, F.; Nieto, R.; Trigo, R.; Drumond, A.; Reason, C.; Taschetto, A.; Ramos, A.; Kumar, R.; Marengo, J. Major Mechanisms of Atmospheric Moisture Transport and Their Role in Extreme Precipitation Events. *Annu. Rev. Environ. Resour.* **2016**, *41*, 117–141. [CrossRef]
68. Viale, M.; Valenzuela, R.; Garreaud, R.D.; Ralph, F.M. Impacts of Atmospheric Rivers on Precipitation in Southern South America. *J. Hydrometeorol.* **2018**, *19*, 1671–1687. [CrossRef]
69. Anselmo, E.M.; Machado, L.A.T.; Schumacher, C.; Kiladis, G.N. Amazonian mesoscale convective systems: Life cycle and propagation characteristics. *Int. J. Climatol.* **2021**, *41*, 3968–3981. [CrossRef]
70. Anselmo, E.M.; Schumacher, C.; Machado, L.A. The Amazonian low-level jet and its connection to convective cloud propagation and evolution. *Mon. Weather. Rev.* **2020**, *148*, 4083. [CrossRef]
71. Bendix, J.; Rollenbeck, R.; Göttlicher, D.; Cermák, J. Cloud occurrence and cloud properties in Ecuador. *Clim. Res.* **2006**, *30*, 133–147. [CrossRef]
72. Torrealba, E.; Amador, J. La corriente en chorro de bajo nivel sobre los Llanos Venezolanos de Sur América. *Rev. Climatol.* **2010**, *10*, 1–20.
73. Silva Dias, M.; Silva Dias, P.; Longo, M.; Fitzjarrald, D.R.; Denning, A.S. River breeze circulation in eastern Amazonia: Observations and modelling results. *Theor. Appl. Climatol.* **2004**, *78*, 111–121. [CrossRef]
74. dos Santos, M.J.; Silva Dias, M.A.; Freitas, E.D. Influence of local circulations on wind, moisture, and precipitation close to Manaus City, Amazon Region, Brazil. *J. Geophys. Res. Atmos.* **2014**, *119*, 13–233. [CrossRef]
75. Santos, M.J.; Medvigy, D.; Silva Dias, M.A.; Freitas, E.D.; Kim, H. Seasonal flooding causes intensification of the river breeze in the Central Amazon. *J. Geophys. Res. Atmos.* **2019**, *124*, 5178. [CrossRef]
76. Silva Dias, M.A.F.; Petersen, W.; Silva Dias, P.L.; Cifelli, R.; Betts, A.K.; Longo, M.; Gomes, A.M.; Fisch, G.F.; Lima, M.A.; Antonio, M.A.; et al. A case study of convective organization into precipitating lines in the Southwest Amazon during the WETAMC and TRMM-LBA. *J. Geophys. Res. Atmos.* **2002**, *107*, LBA 46-1–LBA 46-15. [CrossRef]
77. Carvalho, L.M.; Jones, C.; Silva, D.M. Intraseasonal large-scale circulations and mesoscale convective activity in tropical South America during the TRMM-LBA campaign. *J. Geophys. Res. Atmos.* **2002**, *107*, 1–9. [CrossRef]
78. Carvalho, L.M.V.; Jones, C.; Liebmann, B. The South Atlantic Convergence Zone: Intensity, Form, Persistence, and Relationships with Intraseasonal to Interannual Activity and Extreme Rainfall. *J. Clim.* **2004**, *17*, 88–108. [CrossRef]
79. Vera, C.; Baez, J.; Douglas, M.; Emmanuel, C.B.; Marengo, J.; Meitin, J.; Nicolini, M.; Nogues-Paegle, J.; Paegle, J.; Penalba, O.; et al. The South American Low-Level Jet Experiment. *Bull. Am. Meteorol. Soc.* **2006**, *87*, 63–78. [CrossRef]
80. Assunção, R.M.; Neves, M.C.; Câmara, G.; Da Costa Freitas, C. Efficient Regionalization Techniques for Socio-Economic Geographical Units Using Minimum Spanning Trees. *Int. J. Geogr. Inf. Sci.* **2006**, *20*, 797–811. [CrossRef]
81. De la Cruz, G.; Huerta, A.; Espinoza, J.C.; Lavado-Casimiro, W. Present Variability and Future Change in Onset and Cessation of the Rainy Season Over Peru. *Int. J. Climatol.* **2025**, *45*, e8700. [CrossRef]
82. Espinoza, J.C.; Ronchail, J.; Marengo, J.A.; Segura, H. Contrasting north–south changes in Amazon wet-day and dry-day frequency and related atmospheric features (1981–2017). *Clim. Dyn.* **2019**, *52*, 5413–5430. [CrossRef]
83. Cerón, W.L.; Kayano, M.T.; Andreoli, R.V.; Canchala, T.; Avila-Diaz, A.; Ribeiro, I.O.; Rojas, J.D.; Escobar-Carbonari, D.; Tapasco, J. New insights into trends of rainfall extremes in the Amazon basin through trend-empirical orthogonal function (1981–2021). *Int. J. Climatol.* **2024**, *44*, 3955–3975. [CrossRef]
84. Nobre, C.A.; Sellers, P.J.; Shukla, J. Amazonian deforestation and regional climate change. *J. Clim.* **1991**, *4*, 957–988. [CrossRef]
85. Silva Dias, M.A.F.; Rutledge, S.; Kabat, P.; Silva Dias, P.L.; Nobre, C.; Fisch, G.; Dolman, A.J.; Zipser, E.; Garstang, M.; Manzi, A.O.; et al. Cloud and rain processes in a biosphere–atmosphere interaction context in the Amazon region. *J. Geophys. Res. Atmos.* **2002**, *107*, LBA 39-1–LBA 39-18. [CrossRef]
86. Debortoli, N.S.; Dubreuil, V.; Funatsu, B.; Delahaye, F.; de Oliveira, C.H.; Rodrigues-Filho, S.; Saito, C.H.; Fetter, R. Rainfall patterns in the Southern Amazon: A chronological perspective (1971–2010). *Clim. Change* **2015**, *132*, 251–264. [CrossRef]

87. Artaxo, P.; Rizzo, L.V.; Brito, J.F.; Barbosa, H.M.J.; Arana, A.; Sena, E.T.; Cirino, G.G.; Bastos, W.; Martin, S.T.; Andreae, M.O. Atmospheric aerosols in Amazonia and land use change: From natural biogenic to biomass burning conditions. *Faraday Discuss.* **2013**, *165*, 203–235. [CrossRef]

Disclaimer/Publisher's Note: The statements, opinions and data contained in all publications are solely those of the individual author(s) and contributor(s) and not of MDPI and/or the editor(s). MDPI and/or the editor(s) disclaim responsibility for any injury to people or property resulting from any ideas, methods, instructions or products referred to in the content.